

## Article

# Geochemistry, Mineralization, and Fluid Inclusion Study of the Bayan-Uul Porphyry Au-Cu-(Mo) Deposit, Central Mongolia

Bolor-Erdene Bilegsaikhan <sup>1,\*</sup>, Kotaro Yonezu <sup>2</sup>, Jargalan Sereenen <sup>3</sup> , Oyungerel Sarantuya <sup>1</sup> and Baasanjargal Borshigo <sup>4</sup>

<sup>1</sup> School of Geology and Mining Engineering, Mongolian University of Science and Technology, Ulaanbaatar 14191, Mongolia; oyungerel\_s@must.edu.mn

<sup>2</sup> Department of Earth Resource Engineering, Kyushu University, Fukuoka 819-0395, Japan; yone@mine.kyushu-u.ac.jp

<sup>3</sup> Center for Research and Innovation in Technology Minerals, Mongolian University of Science and Technology, Ulaanbaatar 14191, Mongolia; jargalan@must.edu.mn

<sup>4</sup> Millennium Storm LLC, 20 Baruun Selbe, 5th Khoroo, Chingeltei District, Ulaanbaatar 15171, Mongolia; baasanjargal@mstorm.mn

\* Correspondence: bolor-erdene@must.edu.mn

**Abstract:** The Bayan-Uul porphyry Au-Cu-(Mo) deposit occurs within the Mongol–Okhotsk Orogenic Belt, which is a part of the Central Asian Orogenic Belt. To understand geotectonic, petrogenesis, mineralization, and ore-forming fluid evolution of the Bayan-Uul deposit, we report petrographic and geochemical analyses of host rocks, mineralogy of ores, and fluid inclusion characteristics. Based on petrographic and mineralogical analyses, Cu, Mo, and Au mineralization occurs as disseminated and sulfide-bearing quartz–tourmaline veins hosted within granodiorites, monzodiorites, and diorite porphyry and tourmaline breccia. Four main alteration assemblages are identified: potassic, phyllic, argillic, and quartz–tourmaline alteration. The ore mineralogy of quartz–tourmaline veinlets are classified into A-type veinlets (quartz + tourmaline + chalcopryrite + magnetite + pyrite ± electrum), B-type veinlets (quartz + tourmaline + molybdenum + chalcopryrite + pyrite), and C-type veinlets (quartz + tourmaline + pyrite ± chalcopryrite). Fluid inclusions are found in quartz–tourmaline veinlets consisting mainly of liquid-rich two-phase (L-type), vapor-rich two-phase (V-type), and solid-bearing multi-phase (S-type) inclusions. The homogenization temperatures for the fluid inclusions in A-type, B-type, and C-type veinlets range from 215 to 490 °C, 215 to 500 °C, and 160 to 350 °C and their salinity varies from 5.4 to 43.5 wt.%, 16 to 51.1 wt.%, and 3.4 to 24.1 wt.% NaCl equivalent, respectively. Coexistence of (L-type), (V-type), and (S-type) inclusions support fluid boiling. The  $\delta^{18}\text{O}$  values of ore fluids from different mineralizing A-, B-, and C-type veins are 8.7‰, 10.9‰, and 8.4‰, respectively, and the  $\delta^{34}\text{S}$  values of sulfide minerals range from –1.4‰ to 5.3‰, which indicates magmatic origin.



**Citation:** Bilegsaikhan, B.-E.; Yonezu, K.; Sereenen, J.; Sarantuya, O.; Borshigo, B. Geochemistry, Mineralization, and Fluid Inclusion Study of the Bayan-Uul Porphyry Au-Cu-(Mo) Deposit, Central Mongolia. *Minerals* **2024**, *14*, 320. <https://doi.org/10.3390/min14030320>

Academic Editor: David Lentz

Received: 2 January 2024

Revised: 23 February 2024

Accepted: 23 February 2024

Published: 20 March 2024

**Keywords:** Bayan-Uul; porphyry Au-Cu-(Mo); fluid evolution; alterations; inclusions



**Copyright:** © 2024 by the authors. Licensee MDPI, Basel, Switzerland. This article is an open access article distributed under the terms and conditions of the Creative Commons Attribution (CC BY) license (<https://creativecommons.org/licenses/by/4.0/>).

## 1. Introduction

Porphyry Cu systems are the source of more than 60% of the world's Cu and more than 90% of its Mo, as well as most of the Re, considerable amounts of Au, and minor amounts of Ag, Pd, Te, Bi, Se, Zn, and Pb [1]. A number of conditions must be met during the evolution of a magmatic–hydrothermal system in order to produce an economically viable deposit, namely, partial melting of the mantle through magma ascent, differentiation, emplacement in the crust, fluid exsolution, and, finally, mineral precipitation from a hydrothermal system [1–3].

In Mongolia, porphyry Cu deposits and the mining of copper, as well as its byproducts, are a key factor to the country's economic growth. The Oyu-Tolgoi porphyry Cu-Au deposit in southern Mongolia and the Erdenet porphyry Cu-Mo deposit in northern Mongolia are

the two main porphyry Cu activities that are now in operation. The Bayan-Uul porphyry Au-Cu-(Mo) is the first deposit discovered in the central Mongolian region, and is currently in the exploration phase. The total resource and reserves of the Oyu-Tolgoi porphyry Cu-Au deposit is 6.382 Gt at 0.67% Cu and 0.29 g/t Au, as well as 1.494 Gt at 0.85% Cu, 0.31 g/t Au and 1.23 g/t Ag (Rio Tinto annual report, 2015). The Erdenet porphyry Cu-Mo deposit's measured, indicated, and inferred resource and reserves are 2.261 Bt at 0.25% Cu and 0.015% Mo [4].

The Bayan-Uul porphyry Au-Cu-(Mo) deposit is located at 46°45'00" N and 104°46'00" E in the Tov province, about 200 km southwest of Ulaanbaatar, the capital of Mongolia (Figure 1). The first geological survey at a scale of 1:1,500,000 was conducted by Russian scientists in 1966 and noted the presence of quartz–tourmaline–galena–chalcopyrite assemblage in the Bayan-Uul deposit region. During the 1970s and 1980s, joint Russian and Mongolian geological teams mapped at scales of 1:200,000 and 1:50,000 as well as partly detailed geological mapping at a scale of 1:10,000 in the deposit area.

Koval et al. [5], conducted the exploration geochemistry survey and surficial geological observation including a geophysical survey. They noted that the host rocks of the Bayan-Uul porphyry deposit are relatively high potassium calc-alkaline rocks and affected by epidote–chlorite, quartz–sericite, and quartz–tourmaline alteration, and argillic alteration were observed on the surface. They demonstrated the general distribution of elements based on the geochemical properties of the surface and mentioned that the magmatic associations and hydrothermal alterations of the Bayan-Uul deposit are similar to porphyry-type copper mineralization. In addition, Ariunbileg et al. [6] briefly characterized the relationship between Cu-Au mineralization and quartz–tourmaline stockwork of the Bayan-Uul porphyry deposit. Cox and Lamb [7] reported new  $^{40}\text{Ar}/^{39}\text{Ar}$  age data for some porphyry Cu deposits of Mongolia. They stated that the Bayan-Uul porphyry Cu deposits  $^{40}\text{Ar}/^{39}\text{Ar}$  age spectrum shows 220–223 Ma in biotite and plagioclase from biotite granodiorite. The Re-Os age of disseminated molybdenite in the host rock shows 227.2 Ma [8].

Although studies of geochemical and hydrothermal alteration of the Bayan-Uul porphyry deposit have been conducted, these have mostly been done on surface samples. Therefore, there is a lack of whole-rock major and trace-element geochemistry, detailed hydrothermal alteration, and ore mineralization. Fluid inclusion and O and S isotope analysis have not been conducted before. The main goals of this research are (i) to characterize the petrogenesis of host rocks and to present the tectonic relationship of the Bayan-Uul deposit and Mongol–Okhotsk Orogenic Belt based on geochemistry analysis, and (ii) to report developed characteristics of the Bayan-Uul deposit in terms of porphyry-type hydrothermal alteration, mineralization, and fluid inclusion.

## 2. Regional Geology

The Bayan-Uul deposit is located in the Khentey-Khangay (or Hangay-Hentey) granitoid belt of Paleozoic to Mesozoic ages within north-central Mongolia (Figure 1) that extends to the Sea of Okhotsk, Angara-Vitim, and Erguna Massifs, in the territories of Russia and China. This granitoid belt in Mongolia intruded sedimentary successions within the Khentey-Khangay basin, interpreted as a Devonian–Carboniferous accretionary wedge at the northern margin of the Mongol–Okhotsk Orogenic Belt, which represents the youngest and enigmatic part within the Central Asian Orogenic Belt (CAOB) [9,10]. The CAOB is considered as the longest-lasting continental growth since the Neoproterozoic until the Permian, extending from the Ural Mountains in the west to the Pacific Ocean in the east and from the Siberian Craton in the north to the Tarim and northeast China (or Sino-Korean) Cratons in the south [11]. The CAOB has been formed by the successive accretions of island arcs and microcontinents, ophiolites, oceanic islands, seamounts, accretionary wedges, and oceanic plateaus that prevailed within the Paleo-Asian Ocean.

The northern domain of Mongolia, which marks the Late Cambrian–Ordovician peri-Siberian collage and is separated from the south domain by the Main Mongolian Lineament [11] is crosscut by the younger Mongol–Okhotsk Orogenic Belt (MOB; Figure 1),

which formed following the subduction and closure of the MOO [9,12]. The MOB extends more than 3000 km from central Mongolia to the Uda Gulf in the Okhotsk Sea in the northeast [9,13]. The MOB formed during the closure of the MOO, which led to the collision of the Siberian Craton and the Amur Block during the Middle Jurassic–Early Cretaceous [14–16]. Researchers suggest that the MOO subducted both to the north underneath the Siberian craton [12] and to the south underneath the Amur block [17–19] in a scissor-like manner, younging from west to east based on the ages of granitoids that occur alongside the MOB, although south of the MOB does not necessarily have the younging trend from west to east [12]. The Khentey-Khangay granitoids and batholiths distributed in central and northern Mongolia and Transbaikalia indicate the northward subduction of the MOO underneath the Siberian Craton started in the Devonian and lasted until the Late Triassic–Early Jurassic [12,20,21]. The southward subduction of the MOO is suggested to have started in the Carboniferous and the main subduction-related magmatism occurred during the Permian–Early Jurassic based on the granitoids distributed in central and northeast Mongolia, northeast China, and east Russia [22–25].

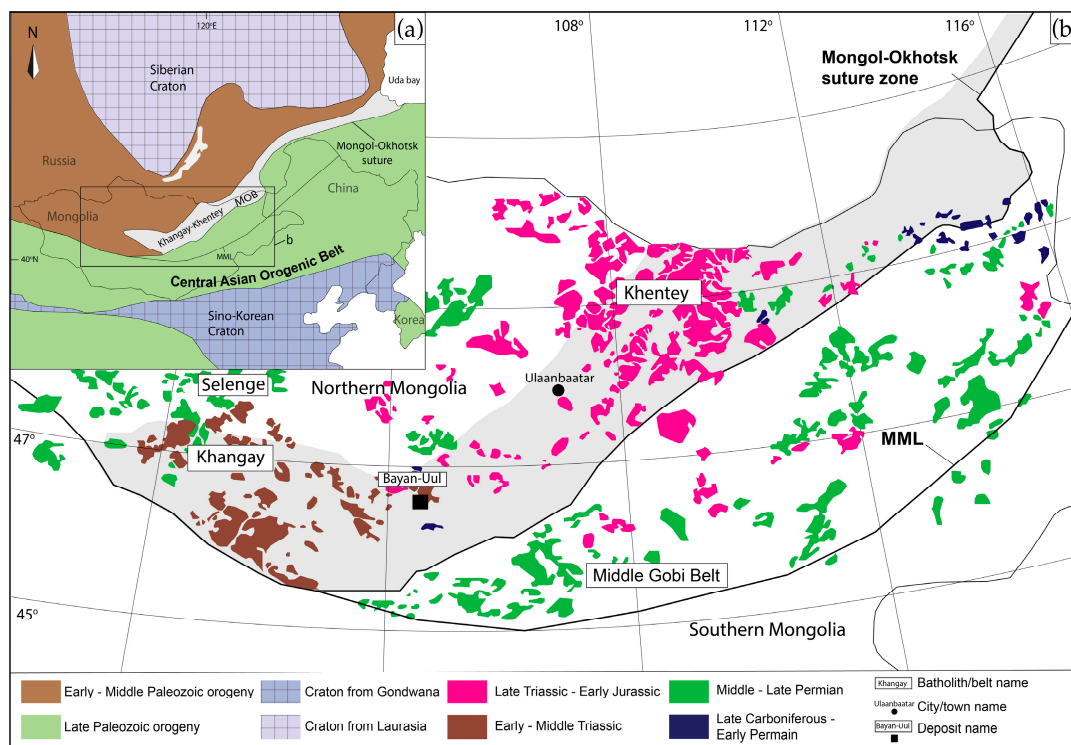


**Figure 1.** (a) Location of large granitic batholiths in the eastern segment of the CAOB [26]. (b) Late Paleozoic–Early Mesozoic granitoid distribution in central and northeastern Mongolia. Shaded area outlines the Khentey-Khangay basin, modified after [24].

### 3. Deposit Geology

The deposit area is composed of the Silurian unclassified sedimentary rocks, the Lower-Middle Devonian Khurentolgoi Formation, and the Late Triassic Bayan-Uul Formation that are intruded by the Late Permian–Early Triassic Delgerkhaan intrusive complex and Late Triassic to Early Jurassic Bayan-Uul porphyry intrusive complex, all of which are overlain by the Neogene–Quaternary loose sediments (Figure 2). The geological age of the above rocks, formations, and complexes are not an absolute age, and the age is determined by geological relationships and age analysis conducted in other areas of same formation.

The Silurian unclassified rocks consist of quartz–chlorite–sericite–phyllite schist, quartz–chlorite–epidote schist, actinolite–hornblende green schist, schistose sandstone, and siltstone [27,28]. The Silurian unclassified rocks intruded by Late Permian–Early

Triassic Delgerkhaan intrusive complex near the Khar Toirom hill are unconformably overlain by Upper Triassic Bayan-Uul Formation fossil-bearing sediments around Javkhlant Mountain [29].

The Lower to Middle Devonian Khurentolgoi Formation is distributed at the northern part of the deposit area and subdivided into two members based on lithology [28]. The lower member is composed of dark gray sandstone, siltstone, and conglomerate, and the upper member consists of sandstone, siltstone, coarse-grained sandstone, cherty-quartzite, and metabasalt [28]. The Khurentolgoi formation sediments are cut by the Late Permian–Early Triassic Delgerkhaan intrusive complex and the Late Triassic–Early Jurassic Bayan-Uul porphyry intrusive complex.

The Late Triassic Bayan-Uul Formation consists of three members. The lower member consists of tuffogenic conglomerate, interlayered with volcanomict sandstone, siltstone, basalt, and andesitic basalt with thickness ranging from several cm to 100 m [28]. The middle member is composed of andesite, trachyandesite, andesitic basalt, andesitic dacite, and their tuffs. The upper member is similar to the lower member, but contains diabases with thicknesses of up to 85 m [27,28,30]. The Bayan-Uul Formation sediments are cut by the Late Triassic–Early Jurassic Bayan-Uul porphyry complex [27,28,30].

Late Permian–Early Triassic Delgerkhaan intrusive complex is divided into four phases, and the first and second phases are distributed around the Bayan-Uul deposit area [29]. The first phase is medium-grained monzodiorite, quartz–monzodiorite and monzogabbro, and the second phase is medium- to coarse-grained porphyric biotite, biotite–hornblende granodiorite, and granite [27–29]. According to reports [24], the U–Pb concordia age of Delgerkhaan intrusive complex zircon is  $220 \pm 2$  Ma.

Late Triassic–Early Jurassic Bayan-Uul porphyry is divided into two phases. The first phase is medium-grained granite, partly fine-grained biotite granite, and porphyric alkaline granite. The second phase usually forms small stocks along the fault zone and consists of granite porphyry, granodiorite porphyry, quartz diorite porphyry, and quartz monzodiorite porphyry. The second phase is spatially associated with porphyry mineralization.

The Bayan-Uul deposit area is intensively disturbed by fault systems, which are identified as early Paleozoic (Band-Uul) and Mesozoic (Ulaan Del), including some small faults in various directions [31]. The Band-Uul fault is the oldest and strikes in a southeast to northwest direction, forming a 40 km long and 2–5 km wide zone [31]. The fault originated in the Early Paleozoic period and was most active during the Triassic–Jurassic, then the intensity gradually weakened in the Cretaceous [27,28]. The Mesozoic Ulaan Del fault forms a structure trending northeast to southwest, forming a 0.7–2.0 km wide and 28 km long zone, identified to be a pathway of the emplacement of the Bayan-Uul porphyry complex as well as Au–Cu–(Mo) mineralization [27,28], (Figure 2).

### 3.1. Bayan-Uul Porphyry Complex

The Bayan-Uul porphyry complex forms small to medium intrusive bodies with various morphological shape and composed of monzodiorite, diorite porphyry, and granodiorite [27,28] (Figure 3). Monzodiorite is medium- to coarse-grained, pinkish-grey to pinkish-red in color, abundant in potassium feldspar, plagioclase, and biotite with a low amount of quartz, and contains sulfide minerals such as chalcopyrite, pyrite, and molybdenite. Monzodiorite is locally altered and quartz–tourmaline, phyllic, and potassic alteration are identified in the drill holes (ex. BDH-78) (Figure 4a). Diorite porphyry is medium- to coarse-grained with porphyritic texture, and composed of plagioclase, quartz, potassium feldspar, and biotite with a minor amount of sulfides (Figure 4b,c). Granodiorite is fine- to medium-grained, composed of plagioclase, quartz, hornblende, potassium feldspar, and lesser biotite. It locally shows potassic and quartz–tourmaline alteration. The granodiorite is extensively cut by sheeted veins and stockworks of sulfide-bearing quartz–tourmaline and tourmaline veinlets (Figure 4d).

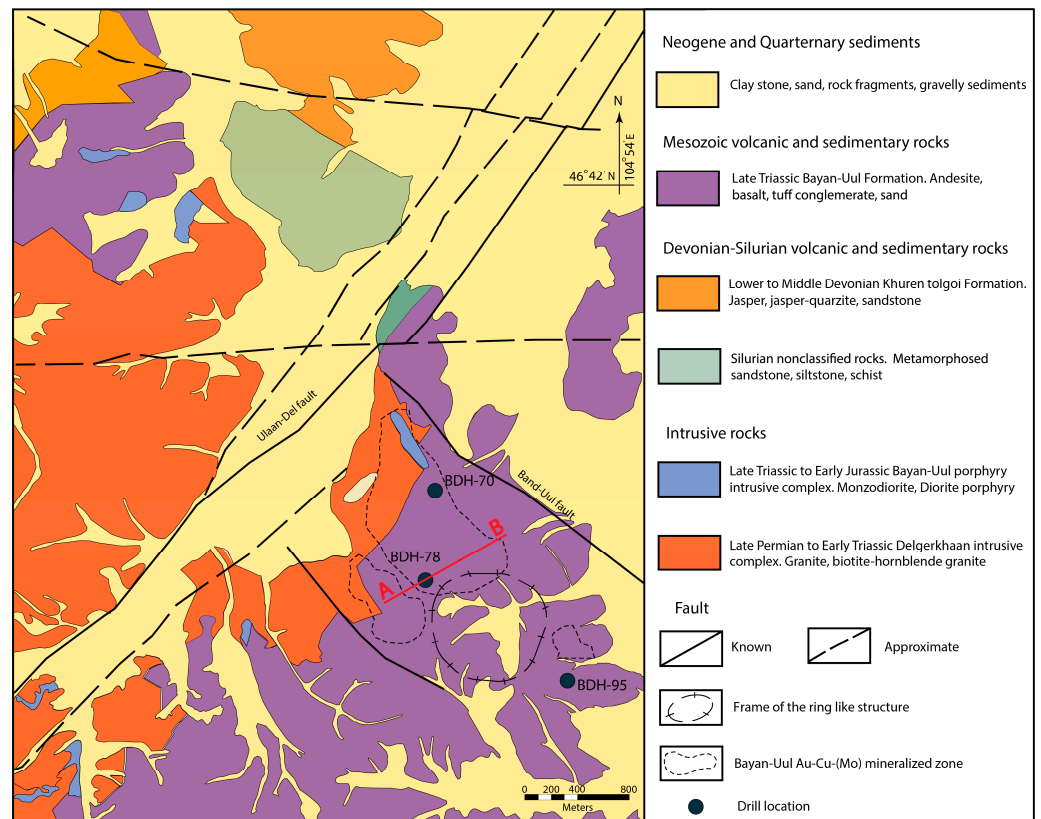


**Figure 2.** Geological map of the Bayan-Uul porphyry deposit, modified after [31]. A-B shows the cross section of the figure below.

According to the field observations, the monzodiorite is widely distributed comparing to the granodiorite and diorite porphyry, and it forms mostly dyke-shaped bodies with a northwest direction (Figure 4d).

### 3.2. Gold, Copper and Molybdenum Mineralization

The previous studies reported that the Bayan Uul deposit is characterized as the diatreme breccia pipe and porphyry system with one km diameter overlain by lithocap, including pyrite-rich sericitic, argillic, and quartz–tourmaline alteration, representing a shallow erosion level [31]. The lithocap is characterized by a ring-shaped structure 8 km in diameter (Figure 2).

Gold–copper–(Mo) mineralization of the Bayan Uul deposit is mainly associated with the quartz–tourmaline veins, quartz–tourmaline veining zones, and brecciated quartz–tourmaline zones on the surface as well as in drill holes. According to the field observations, ore minerals present malachite, pyrite, hematite, magnetite, chalcopyrite, and rarely molybdenite in the outcrops as well as drill cores (Figure 5a,b). Most of the ore minerals occur within quartz–tourmaline veins and veinlets and quartz–tourmaline breccias, as well as fracture-fillings and fine disseminations within the Bayan Uul porphyry complex. Copper and Mo mineralization mainly occurs as a fine dissemination within veins and veinlets, as well as stockwork within monzodiorite, diorite porphyry, and granodiorite. Gold–Copper–(Mo) mineralization is intersected at depths of 450–1100 m in drill cores, as sheeted quartz–tourmaline veins, veinlets, and stockworks in potassic- and phyllic-altered monzodiorite, diorite porphyry, and granodiorite.

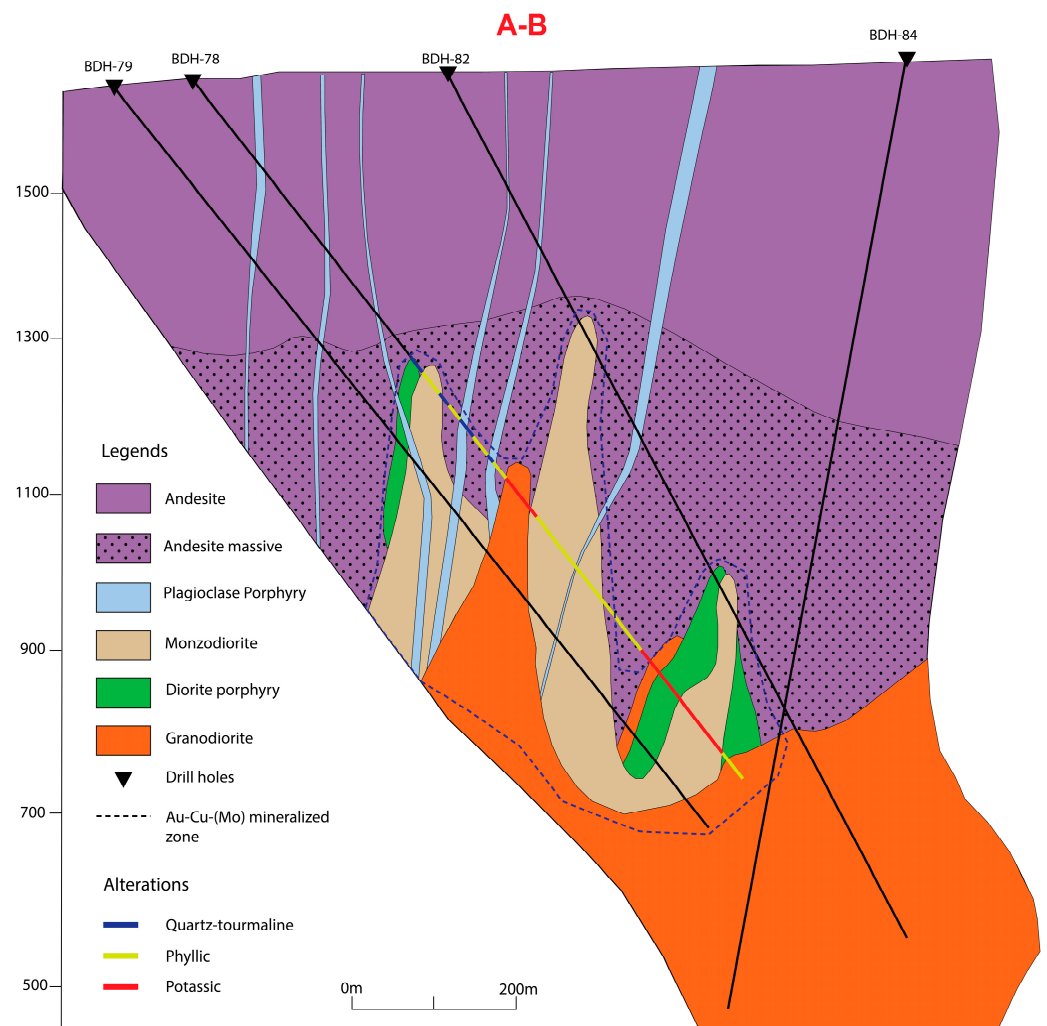


**Figure 3.** Map illustrating the cross-sectional distribution of host rocks, modified after [31], from drill holes BDH-79, BDH-78, BDH-82, and BDH-84. A-B shows the cross section of the figure above.

### 3.3. Alteration and Vein Types

Based on observation of the drill core and outcrop samples, several types of hydrothermal alterations, such as potassic, phyllic, argillic, silicic, and quartz–tourmaline alterations, are identified with a zonal distribution around the center of the mineralized zone of Bayan-Uul porphyry deposit.

Potassic alteration occurs only in the drill core at depths of 750–880 m and is represented by K-feldspar + biotite + magnetite ± chlorite ± sericite assemblages in the granodiorite, diorite porphyry, and monzodiorite. Because of potassic alteration, host rocks are dark- and reddish-pink in color (Figure 5c).

Argillic alteration is identified both in the surface exposures and in the drill cores at shallow depths, and infrequently found as overlapping of the phyllic, potassic alteration in the drill core. Argillic alteration is characterized by kaolinite + alunite + quartz with lesser amounts of sericite and chlorite. It is developed in andesitic rocks near the lithocap area (Figure 5d).

Phyllic alteration occurs in the drill core at depths of ~410–430 m, 460–480 m, 520–680 m, and 700–750 m, as well as at 880–1070 m, overprinting some part of the potassic and quartz–tourmaline alteration. Phyllic alteration is characterized by quartz + pyrite + chlorite + sericite ± chalcopyrite ± magnetite assemblages. Due to the continuous destruction of silicate minerals except for quartz, host rocks strongly suffer from sericite replacement

and are mainly whitish-grey and greenish in color with slightly reddish spots because of K-feldspar (Figure 5e).

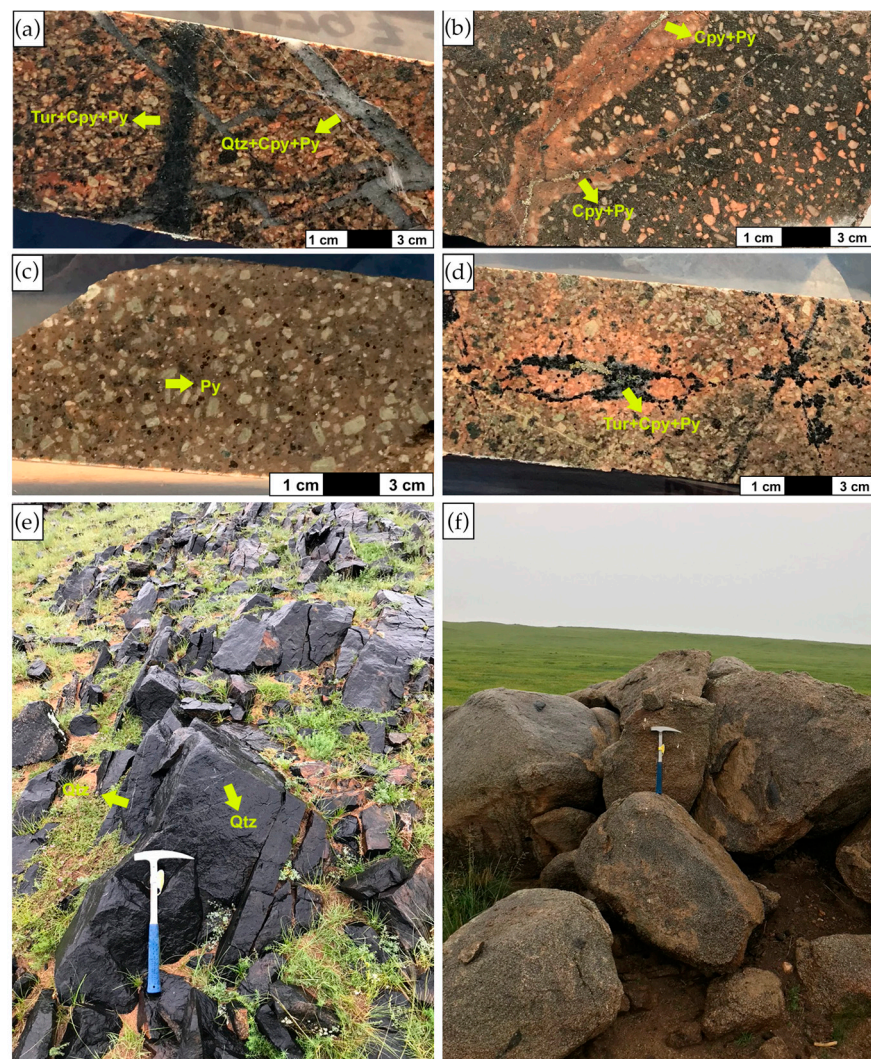


**Figure 4.** Intrusive rock types found within the Bayan-Uul porphyry Au-Cu-(Mo) deposit area. (a) Quartz–sulfide and tourmaline veins within monzodiorite (sample ID: BDH-78-35\_779m). (b) Chalcopyrite and pyrite mineralization associated with diorite porphyry (sample ID: BDH-78-11\_465m). (c) Disseminated pyrite associated with diorite porphyry (sample ID:BDH-78-26\_653m). (d) Tourmaline–sulfide within granodiorite (sample ID: BDH-78-18\_527m). (e) Quartz veins cut the dyke-shaped monzodiorite. (f) Granodiorite outcrop in the Bayan-Uul porphyry Au-Cu-(Mo) deposit area. Abbreviations: Cpy = chalcopyrite, Py = pyrite, Tur = tourmaline, Qtz = quartz.

Abundant silicic leached rocks were found forming the lithocap. Silicic alteration is characterized by quartz + sericite. Silicification was observed on the whole rock mass of the porphyry intrusion or the marginal part of the quartz, quartz–tourmaline veinlets. Silicified porphyry intrusions are characterized by disseminated, fracture-filling quartz and quartz–tourmaline veinlets with sulfide minerals, including dominantly pyrite, and rarely chalcopyrite and molybdenite. Silicic alteration is widely distributed (Figure 5f) and they partly associated with phyllic and quartz–tourmaline alteration.

One of the distinguishable features of the Bayan-Uul deposit compared to the other porphyry deposit in Mongolia is its intense tourmaline alteration. Tourmaline alteration exists as several types, including tourmaline breccia, quartz–tourmaline veinlet, and disseminated as radial textured grains in host rocks. The tourmaline breccias are altered by intense

argillic alteration and contain chalcopyrite, magnetite, and pyrite (Figure 5g). The copper grade of tourmaline breccia is higher than the other host rocks in the Bayan-Uul deposit.

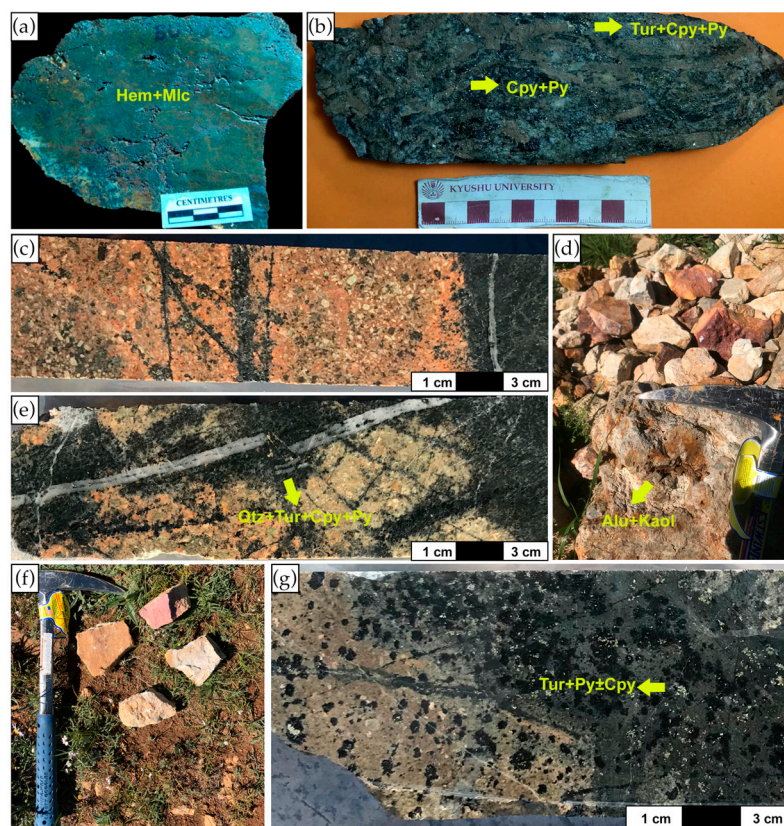


**Figure 5.** Ore minerals and alteration types found within the Bayan-Uul porphyry Au-Cu-(Mo) deposit. (a) Hematite and malachite. (b) Tourmaline breccia (sample ID: BDH-95-2\_160m). (c) Quartz-tourmaline veinlets within potassic altered granite (sample ID: BDH-78-21\_567m). (d) Argillic alteration with oxidized sulfide grains in an outcrop. (e) Centerline tourmaline with phyllic alteration zone (sample ID: BDH-78-19\_534m). (f) Silicic leached rocks in the lithocap area. (g) Radial textured and intense quartz-tourmaline altered rock (sample ID: BDH-78-3\_410m). Abbreviations: Hem = hematite, Mlc = malachite, Cpy = chalcopyrite, Py = pyrite, Tur = tourmaline, Qtz = quartz, Alu = alunite, Kaol = kaolinite.

In the quartz-tourmaline, vein type alteration is dominantly associated with C-type veinlets and partly found together with A- and B-type of veinlets containing abundant pyrite and minor chalcopyrite. Quartz-tourmaline alteration is intersected at the depth of 399–410 m, 440–460 m and 480–510 m of drill core BDH-78. Sometimes tourmaline exists at the centerline of quartz veinlets in the potassic alteration zone.

## 4. Materials and Methods

### 4.1. Materials

A total of thirty-nine ore and host rock samples were collected from the drill hole BDH-78 and three tourmaline breccias, and four samples were also taken from BDH-95, BDH-70 (Figure 2), including five samples from outcrop of altered volcanic rocks. For the petrographic observation, 40 thin sections were prepared in the Economic Geology Laboratory, Kyushu University in order to identify rock types, rock-forming minerals, textures, and alteration types, while 20 polished sections were prepared to determine ore mineral assemblages and their textures. Microscopic observation was conducted using a NIKON Eclipse E600 POL microscope, Nikon Corporation, Minato City, Japan, equipped with an AdvanCam-U3II camera, Advanvision Technology Co., Ltd., Tokyo,

Japan, at the Economic Geology Laboratory, Kyushu University. Minerals unidentified by the optic microscopes were further determined using a SUPERSCAN SS-550 scanning electron microscope, Shimadzu Corporation, Kyoto, Japan, equipped with a standardless, energy dispersive X-ray analyzer located in the Center of Advanced Instrumental Analysis, Kyushu University.

## 4.2. Methods

### 4.2.1. Whole Rock Geochemical Analysis

In order to determine the chemical composition of host rocks, including major elements and some trace element, a total of 15 fresh and least altered samples were analyzed by X-ray fluorescence (XRF) analysis using a RIGAKU RIX-3100 spectrometer, Rigaku Corporation, Tokyo, Japan. The samples were ground to make a powder and pressed into pellets. Loss on ignition (LOI) was determined by heating the samples at 1000 °C for 2 h to determine relative loss of weight. XRF analysis on the sample pellets was conducted under 30 kV and 70 mA conditions, and JA-3 andesite was used as a standard sample to check the machine condition. The reference value of JA-3 was used to monitor the precision, yielding an error of less than 5%. The sample weight for XRF was 5 g. The limit of detection for XRF was 10 ppm. Rare earth element (REE) determinations were performed at the Center of Advanced Instrumental Analysis, Kyushu University, using inductively coupled plasma mass spectrometry (ICP-MS), utilizing Agilent Technologies 7500, Agilent Technologies, California, USA. The sample weighed  $0.20 \pm 0.001$  g. In the preparation process, dilute HCL containing REEs was added to aluminum sec-butoxide ( $\text{Al}(\text{O-sec-Bu})_3$ , TBAO) at room temperature, and the solution was stirred for 2 h. Then, tetraethyl orthosilicate ( $\text{Si}(\text{OEt})_4$ , TEOS) and N, N-dimethyl formamide as a solvent was added into the mixed solution and stirred for 1 h at room temperature. A silica sol containing REEs surrounded by aluminum was obtained. The above reactions were carried out in a glove box replaced with  $\text{N}_2$  gas and a humidity of 15% or less. To prompt hydrolysis of TEOS and polymerization of silicic acid, pure water was added to the sol solution and heated to 110 °C for 1 h. To consume the remaining HCL, propylene oxide was added. The sol solution was heated to 160 °C at a heating rate of 1 °C/h to obtain the dry gel. The dry gel was heated to 1000 °C at a heating rate of 10 °C/h in an electric furnace to convert to a hard glass and stood for 2 h at 1000 °C. The concentration of REEs in the glasses was analyzed by ICP-MS after the acid decomposition of the glass. The limit of detection for ICP-MS is 0.25 ppb.

### 4.2.2. Fluid Inclusion Analysis

Different types of quartz veins and veinlets were prepared for fluid inclusion analysis. The doubly polished sections were prepared following sequences: polishing the sample's surface, mounting the polished rock to glass, cutting the sample billet from the glass, then polishing the other side of sample to the required thickness. The measurements were conducted using a Linkam LK600 cooling/heating unit with a Nikon Y-IM microscope at the Economic Geology Laboratory, Kyushu University. The homogenization and the ice melting temperatures were measured at the rate of 1 °C/min. Thermocouples were calibrated at  $-53.2$ ,  $0.0$ , and  $313.5$  °C using the boiling point of the standard materials. The salinity of two-phase fluid inclusions was calculated using the fluid inclusion freezing temperature through the equation provided in [32], based on the freezing-point depression of  $\text{H}_2\text{O}$ – $\text{NaCl}$  solutions, ranging from pure water to the eutectic composition. Salinities of halite bearing three-phase fluid inclusions were calculated using the halite dissolution temperature through the equation reported by [33].

### 4.2.3. O-S Isotope Analysis

Based on the microscopic observation of ore minerals, three samples from A-, B- and C-types of sulfide ore bearing quartz veinlets were chosen for oxygen isotope analysis, and seven sulfide samples of chalcopyrite, pyrite, and molybdenite were chosen for sulfur isotope study. The samples were crushed to the required size, then sorted by grain size;

after that, samples were washed and dried to be ready for separation mineral fraction. A binocular microscope was used to separate the quartz, chalcopyrite, pyrite and molybdenite at the Center for Research and Innovation in Technology Minerals of the Mongolian University of Science and Technology.

Oxygen was extracted from approximately 5 mg of sample at 550–600 °C according to the conventional BrF<sub>5</sub> procedure of [34] and analyzed via dual inlet on a Thermo-Finnigan DeltaPlusXP Isotope-Ratio Mass Spectrometer (IRMS) at the Faculty for Isotope Research, ALS, Canada. The  $\delta^{18}\text{O}$  values are reported using the delta ( $\delta$ ) notation in unit of per mil (‰) relative to Vienna Standard Mean Ocean Water (VSMOW) international standard, with a precision of 0.4‰.

Samples were weighed into tin capsules and the sulfur isotopic composition measured using a MAT 253 Stable Isotope Ratio Mass Spectrometer coupled to a Costech ECS 4010 Elemental Analyzer at the Faculty for Isotope Research, ALS, Canada. The  $\delta^{34}\text{S}$  values were calculated by normalizing the  $^{34}\text{S}/^{32}\text{S}$  ratios in the sample to that in the Vienna Canyon Diablo Troilite (VCDT) international standard. Values are reported using the delta ( $\delta$ ) notation in units of per mil (‰) and are reproducible to 0.2‰.

## 5. Results

### 5.1. Petrography of Intrusive Rocks

Monzodiorite, diorite porphyry, granodiorite, and tourmaline breccia are determined by the microscopic observation (Figure 6). Monzodiorite exhibits phaneritic, frequently porphyritic textures, and is generally composed of plagioclase (40 modal %), K-feldspar (30 modal %), biotite (10 modal %), hornblende (10 modal %), and quartz (10 modal %), including zircon, sphene, apatite etc. as accessories. Plagioclase is medium- to coarse-grained (1–6 mm) and forms subhedral crystals with polysynthetic twinning. K-feldspar is also typically medium-grained (1–2 mm) and shows poikilitic and perthitic textures. Biotite forms medium-grained (0.5–1 mm) anhedral and subhedral grains. Hornblende shows euhedral to subhedral textures with sizes up to 0.6 mm in the longest direction and is locally replaced by chlorite. Quartz is generally anhedral and medium-grained (0.5–1.5 mm) (Figure 6a–c).

Diorite porphyry (Figure 6d) consists of plagioclase (60 modal %), biotite (up to 20 modal %), K-feldspar (10 modal %), quartz (10–5 modal %), and minor hornblende and shows porphyritic texture. Plagioclase is medium- to coarse-grained (0.8–5 mm) and found both in porphyry and ground mass, exhibiting subhedral to anhedral crystals with polysynthetic twinning. K-feldspar is typically medium- to coarse-grained (1–5 mm) with subhedral crystals and exhibits Carlsbad twinning and perthitic textures. Quartz (0.5–1.2 mm) are generally medium-grained, anhedral, and irregular in shape (Figure 6e,f). Biotite (0.5–1 mm) appears as euhedral with distinct cleavage, and some of the biotite is slightly replaced by chlorite (Figure 6e).

Granodiorite consists of plagioclase (40 modal %), K-feldspar (20 modal %), quartz (20–25 modal %) hornblende (10 modal %), and biotite (up to 5 modal %) and is characterized by an phaneritic texture. Plagioclase is mainly medium-grained (1–2 mm), shows subhedral to anhedral crystals, and exhibits polysynthetic twinning. K-feldspar is typically medium-grained (1–1.8 mm) and displays subhedral crystals with Carlsbad twinning (Figure 6h). Quartz is generally medium-grained (0.5–1.5 mm), anhedral and irregular in shape. Hornblende is mainly medium-grained (0.2–1 mm) and shows light to dark green in color with mainly euhedral to subhedral crystals, some of which exhibit simple twinning and are infrequently replaced by chlorite in the phyllic alteration zone. Biotite grains display euhedral to anhedral textures with size varying from 0.5 to 0.9 mm (Figure 6g–i).

Tourmaline breccia consists from rock fragments cemented by tourmaline (Figure 6j). The rock fragments are strongly altered porphyric intrusion containing plagioclase (30 modal %), quartz (30 modal %), tourmaline (25 modal %), micas (15 modal %), and some mineral fragments. Plagioclase and K-feldspar are fractured and indistinguishable due to strong

sericitic and argillic alteration, and tourmalinization. Quartz is fine-grained (0.1–0.5 mm) and angular to sub-rounded in shape (Figure 6k,l).

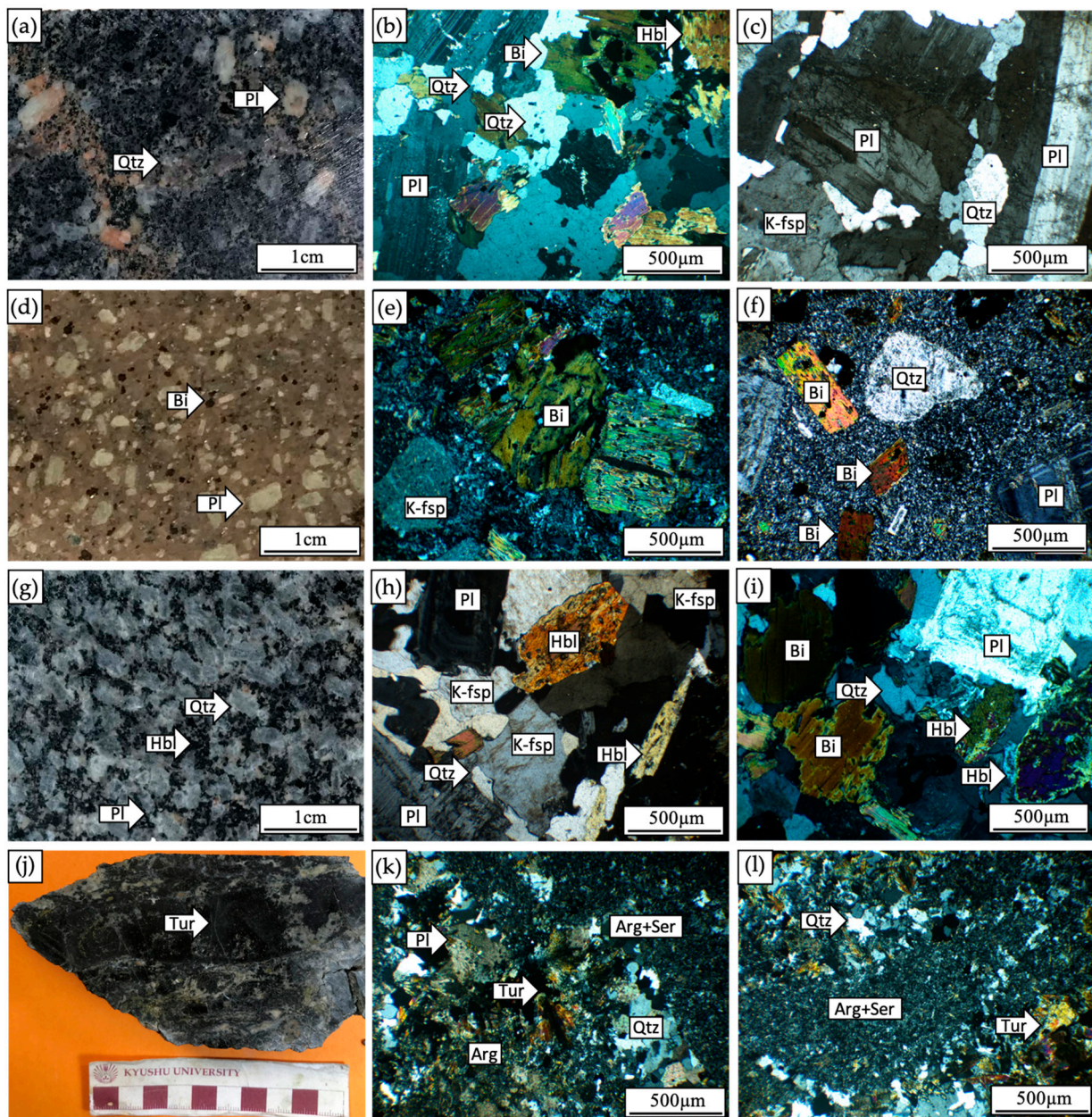


**Figure 6.** Photographs of hand samples and representative transmitted light photomicrographs (crossed polarizers) of the samples from Bayan-Uul porphyry Au-Cu-(Mo) deposit. (a–c) Monzoniorite (sample ID: BDH-78-39\_680m). (d–f) Diorite porphyry, the biotite is slightly replaced by chlorite (sample ID: BDH-78-22\_560m). (g–i) Granodiorite (sample ID: BDH-78-45\_118m). (j–l) Tourmaline breccia (sample ID: BDH-95-3\_150m). Abbreviations: Qtz = quartz, Pl = plagioclase, K-fsp = K-feldspar, Bi = biotite, Hbl = hornblende, Arg = argillic, Tur = tourmaline, Ser = sericite.

Petrography shows that potassic alteration of the Bayan-Uul porphyry deposit consists of K-feldspar + biotite + magnetite ± chlorite ± sericite assemblages. K-feldspar occurs as intergrowth and anhedral crystals (0.5–1 mm) at the marginal part of quartz veinlets and replaced by sericite. Hydrothermal biotite appears medium-grained and occurs similarly as K-feldspar in quartz veinlets (Figure 7a). Phyllic alteration is characterized by intense replacement of plagioclase and K-feldspar by sericite, and biotite is replaced by chlorite (Figure 7c,d). Quartz–tourmaline alteration is characterized by tourmaline and

fine-grained secondary quartz with minor sericite. Tourmaline is the most abundant mineral in the quartz–tourmaline alteration zone and appears as disseminated coarse-grained subhedral radial crystals, or fine-grained mixed with quartz with lower amounts of sericite (Figure 7e,f).

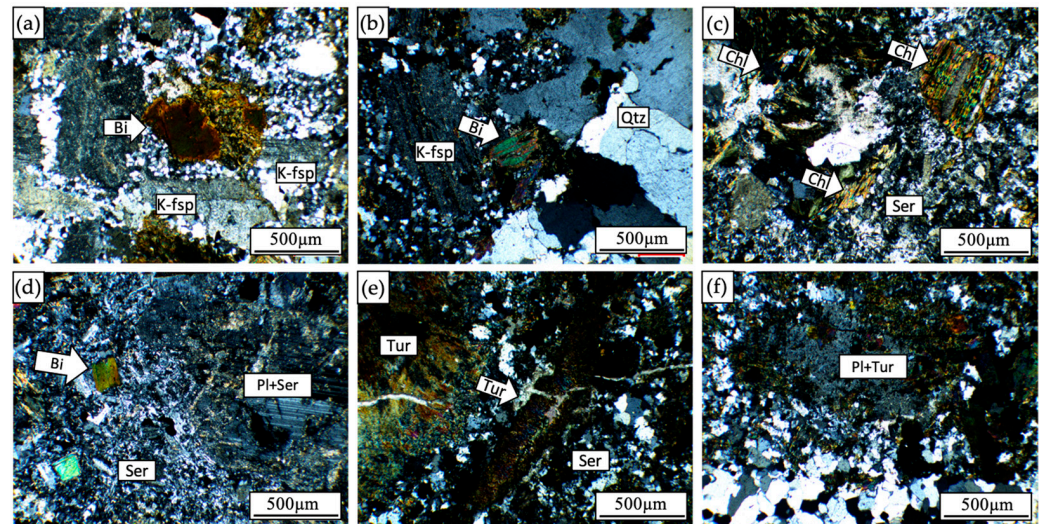


**Figure 7.** Photomicrographs transmitted light (cross-polarized) of alteration minerals (a,b) Potassic alteration. (c,d) Phyllic alteration. (e,f) Quartz–tourmaline alteration. Abbreviations: Qtz = quartz, Pl = plagioclase, K-fsp = K-feldspar, Bi = biotite, Arg = argillic, Tur = tourmaline, Ser = sericite.

## 5.2. Ore Mineralogy

Ore minerals generally occur in fine to coarse grains as a dissemination in the intrusive rocks and associated quartz–tourmaline veinlets. According to the classification of the veinlets by [1,35], A-type, B-type, and C-type veinlets are identified in the Bayan-Uul porphyry deposit (Figure 8). Ore minerals found in the Bayan-Uul porphyry Au-Cu-(Mo) deposit include chalcopyrite, pyrite, molybdenite, and magnetite as dominant ore minerals with a minor presence of electrum and sphalerite. The A-type veinlets are dominated by quartz + tourmaline + chalcopyrite + magnetite + pyrite ± electrum, generally observed in the potassic and phyllic alteration zones (Figure 8a,b). The B-type veinlets are characterized by quartz + tourmaline + molybdenite + chalcopyrite + pyrite and commonly occur in the potassic and phyllic alteration zone (Figure 8b–e). The C-type veinlets consist of quartz + tourmaline + pyrite ± chalcopyrite. These C-type veinlets typically exist in the phyllic and tourmaline-sericitic alteration zones and rarely observed in the potassic alteration zone (Figure 8c–e).

Although gold is the main economic mineral, it was found in small amounts in the selected samples. Based on petrographic observation, electrum was found in association with chalcopyrite in A-type veinlets with subhedral textures with fine-grained sizes up to 0.1 mm (Figure 9a). Chalcopyrite shows a range of forms anhedral textures and irregular shapes with sizes up to 1.5–2 mm. Chalcopyrite is the dominant ore mineral in A-type veinlets, associated with pyrite and molybdenite in B-type veinlets, and infrequently found in C-type veinlets associated with pyrite (Figure 9a–c). Chalcopyrite is mainly associated with pyrite and found to be filling open space cracks (Figure 9e–i). Pyrite is medium- to coarse-grained (0.2–3 mm), forming isometric to irregular crystals (Figure 9c). Pyrite is found in A-type veinlets with chalcopyrite magnetite, B-type veins with molybdenite and chalcopyrite (Figure 9c), and C-type veinlets in arrays or sometimes in association with chalcopyrite (Figure 9d,e). Molybdenite forms aggregates of elongated flakes with needle-like lengths up to 0.4 mm, and is only found in B-type veinlets associated with chalcopyrite (Figure 9f,g). Magnetite grains form in association with chalcopyrite and pyrite in sizes up to 0.4 mm. Magnetite is found in A- and B-type veinlets, associated

with chalcopyrite, pyrite, and rarely molybdenite (Figure 9h). Sphalerite occurs rarely as disseminations in association with chalcopyrite and its size is up to 0.6 mm (Figure 9i).

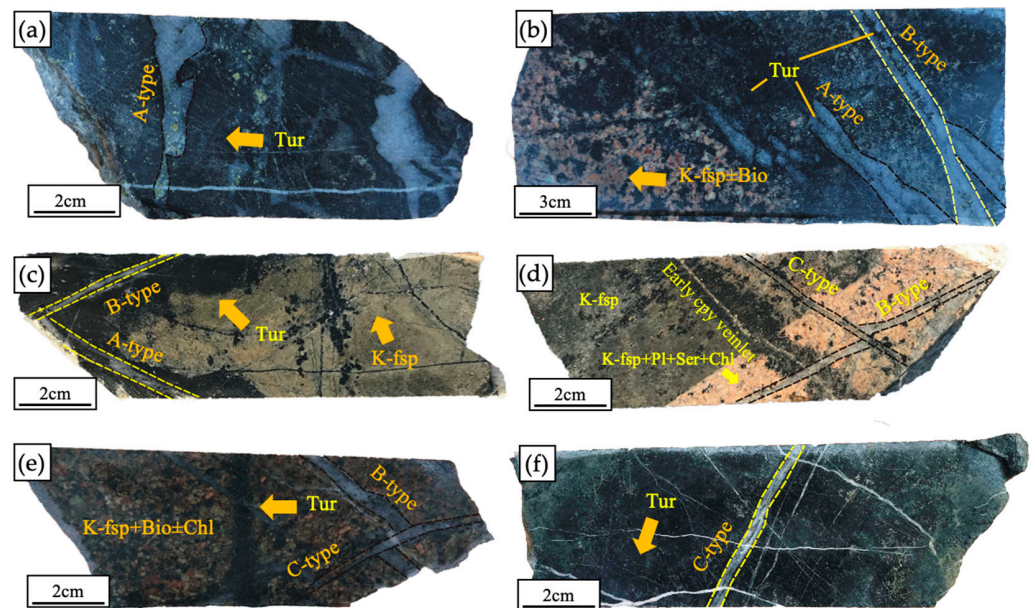


**Figure 8.** Photographs of veinlets cross-cutting relationship. (a) A-type veinlet associated with potassic alteration (sample ID: BDH-78-43\_1007m). (b) A-type veinlet cut by B-type veinlet associated with potassic alteration zone (sample ID: BDH-78-36\_797m). (c) A-type veinlet cut by B-type veinlet associated with phyllic alteration zone (sample ID: BHD-78-30\_690m). (d) Early chalcopyrite veinlet cut by B-type veinlet and B-type veinlet cut by C-type veinlet associated with phyllic alteration zone (sample ID: BHD-78-31\_713m). (e) B-type veinlet cut by C-type veinlet associated with potassic alteration (sample ID: BDH-78-35\_780m). (f) C-type veinlet associated with quartz–tourmaline–sericite alteration zone and cut by the latest non-mineralized calcite veinlets (sample ID: BHD-78-7\_438m). Abbreviations: K-fsp = K-feldspar, Bi = biotite, Tur = tourmaline, Ser = sericite.

### 5.3. Fluid Inclusion Petrography and Microthermometry

Three main types of fluid inclusions have been identified in quartz veins: L-type (liquid-rich) two-phase inclusion, V-type (vapor-rich) two-phase, S-type (halite-bearing) polyphase inclusions, and opaque-bearing fluid inclusions. Based on fluid-inclusion behavior during heating and freezing, the liquid and vapor phase compositions of fluid inclusions were recognized as (H<sub>2</sub>O) in L- and V-type fluid inclusion and the solid phase of S-type fluid inclusions is halite. L-type fluid inclusions are highly variable in shape, from regular ellipsoidal negative crystal to irregular in shape and 5–15 μm in size, with a few observed up to 20 μm (Figure 10a–d). They consist of liquid (H<sub>2</sub>O) and the vapor (H<sub>2</sub>O) phase which occupies between 10 and 40% volume (estimated based on optical methods). They are the most abundant inclusions in A-, B-, and C-type quartz veinlets. V-type fluid inclusions are present in the quartz of A- and B-type early-stage veinlets. They are ellipsoidal, spherical, or irregular negative-crystal in shape and range from 10 to 25 μm. They consist of liquid (H<sub>2</sub>O), and the vapor (H<sub>2</sub>O) phase which occupies >50% volume (Figure 10e–h). S-type fluid inclusions consist of liquid (H<sub>2</sub>O), vapor (H<sub>2</sub>O), and halite (NaCl). The content of the vapor phase varies from 4 to 30% volume. Halite is transparent (no color) and cubic crystal in shape with a 20%–30% volume in all these inclusions (Figure 10g,h). Opaque-bearing fluid inclusions are composed of a transparent daughter crystal, presumably of sulfide minerals, and opaque inclusion phases do not dissolve into inclusion fluids during heating experiments (Figure 10i). Therefore, opaque-bearing fluid inclusions could not be measured and were rarely observed only in the A-type vein.

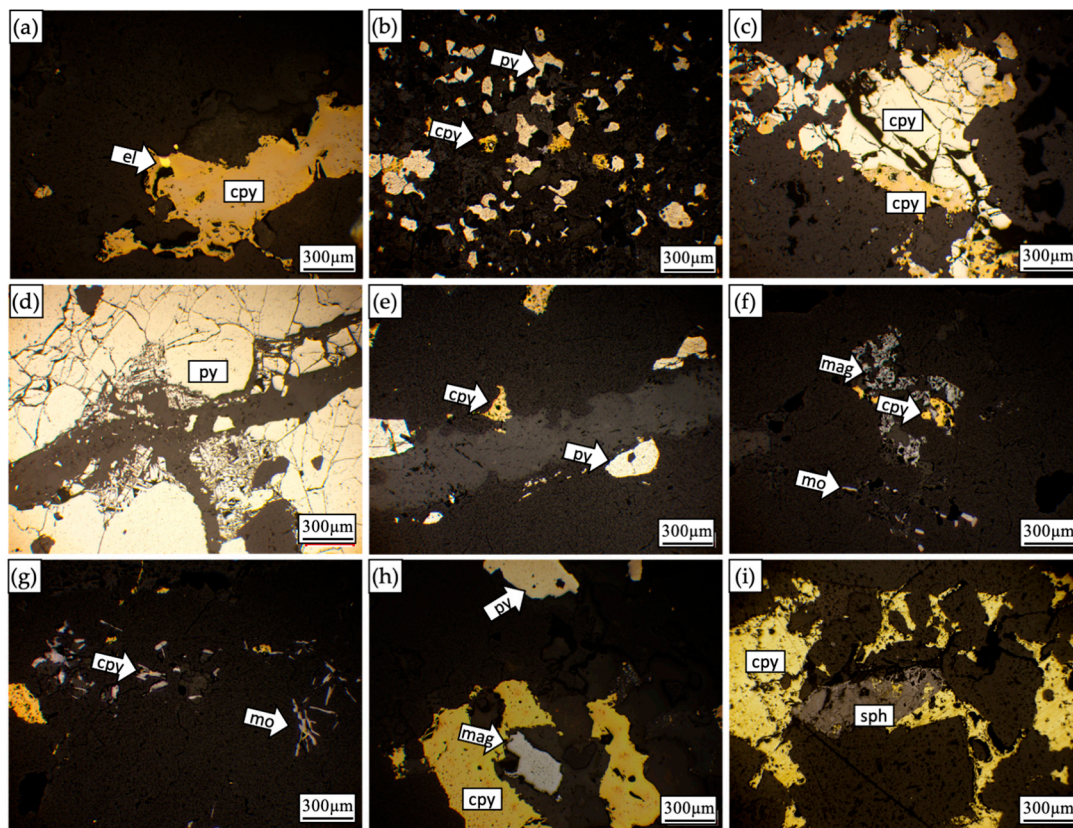


**Figure 9.** Photomicrographs in reflected light. (a) Electrum and chalcopyrite in A-type quartz veinlet hosted in monzodiorite having undergone a phyllic alteration (sample ID: BDH-78-43\_1007m). (b) Disseminated chalcopyrite and pyrite hosted in monzodiorite having undergone a tourmalinization (sample ID: BDH-78-8\_455m). (c) Chalcopyrite and pyrite occurrence in C-type veinlet hosted in monzodiorite having undergone a phyllic alteration zone (sample ID: BDH-78-8\_501m). (d) Pyrite in C-type veinlet hosted in monzodiorite having undergone a quartz–tourmaline alteration (sample ID: BHD-78-14\_489m). (e) Pyrite and chalcopyrite in C-type veinlet hosted in monzodiorite having undergone a quartz–tourmaline alteration (sample ID: BHD-78-7\_438m). (f) Magnetite, chalcopyrite, and molybdenite in B-type veinlet hosted diorite having undergone a potassic alteration (sample ID: BDH-78-35\_780m). (g) Chalcopyrite and molybdenite in B-type quartz veinlet hosted in granodiorite having undergone a potassic alteration (sample ID: BDH-78-36\_797m). (h) Magnetite, pyrite, and chalcopyrite in A-type veinlet hosted in monzodiorite having undergone a phyllic alteration (sample ID: BDH-78-43\_1007m). (i) Chalcopyrite having undergone a sphalerite alteration, hosted in monzodiorite (sample ID: BDH-78-1\_404m). Abbreviations: el = electrum, cpy = chalcopyrite, mo = molybdenite, mag = magnetite, sph = sphalerite.

A-type veinlets (quartz + tourmaline + chalcopyrite + magnetite + pyrite ± electrum) have an abundance of L-type and S-type inclusion with minor V-type inclusions. The homogenization temperature of L-type and V-type inclusions range from 220 to 490 °C and 259 to 395 °C with salinity 9.0–22.5 and 5.4–25.4 wt.% NaCl equivalent, respectively. The homogenization temperature (Th) and halite dissolution temperature (Td) of S-type range from 215 to 362 °C and 228 to 500 °C with 36.2–43.5 wt.% NaCl equivalent, respectively (Figure 11a).

B-type veinlets (quartz + tourmaline + molybdenum + chalcopyrite + pyrite) consist of abundant L-type and S-type inclusions and minor V-type inclusions. The homogenization temperature of L-type and V-type inclusions range from 280 to 377 °C and 333 to 500 °C with salinity 19.5–27.4 and 16–21.7 wt.% NaCl equivalent, respectively. The homogenization temperature (Th) and halite dissolution temperature (Td) of S-type range from 215 to 432 °C and 330–500 °C with 36.2–51.1 wt.% NaCl equivalent, respectively (Figure 11b).

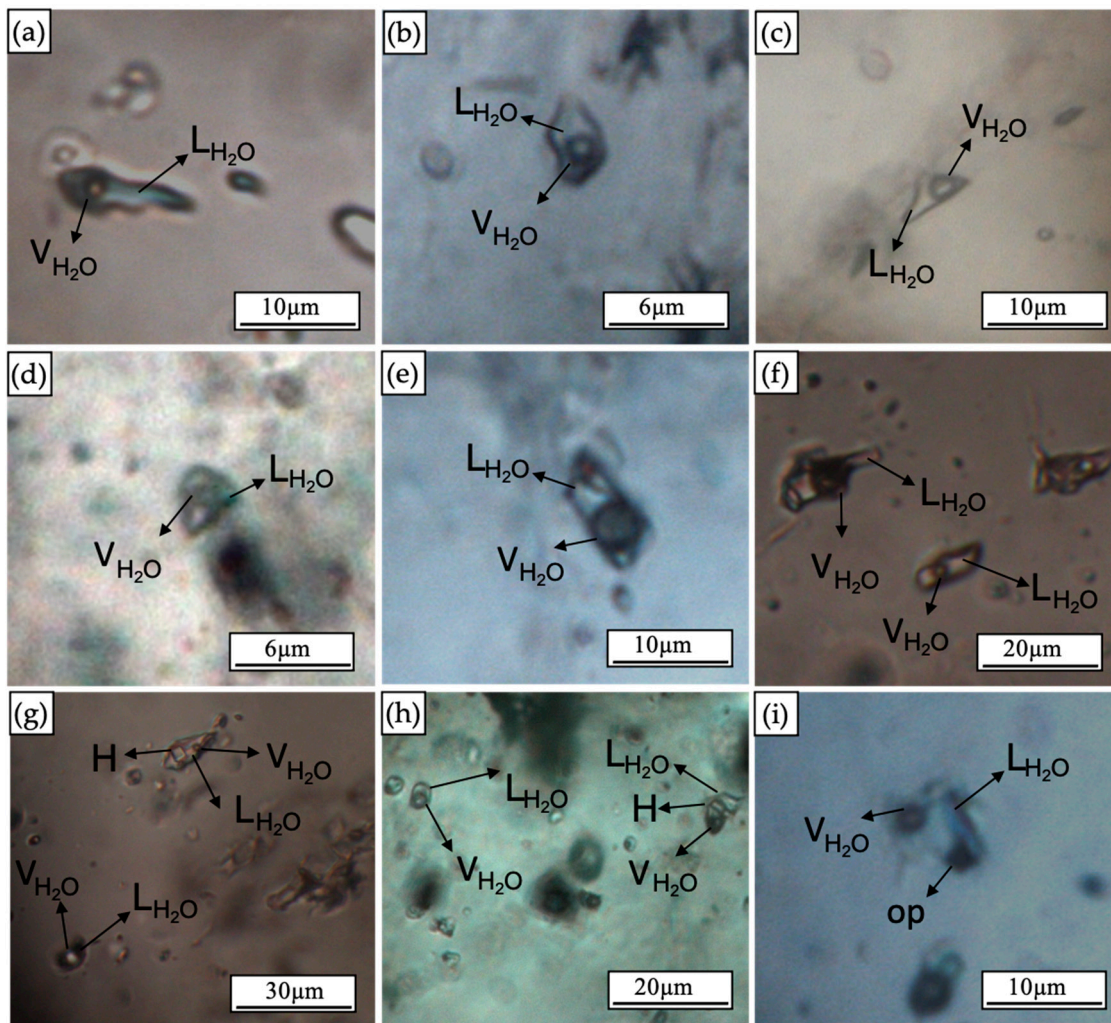


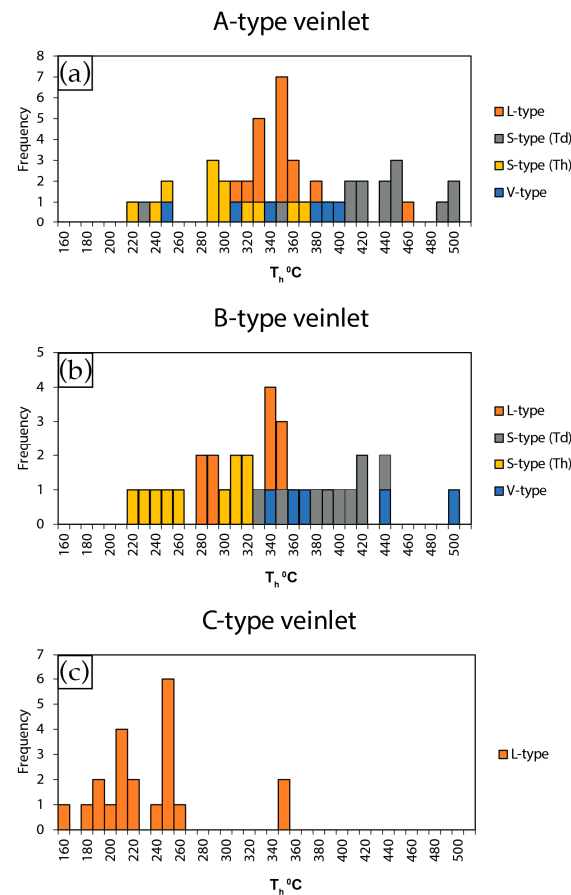
**Figure 10.** Photomicrograph of fluid inclusions in the different types of veinlets of the Bayan-Uul porphyry deposit. (a) L-type fluid inclusion in the A-type quartz veinlet. (b) L-type fluid inclusion in the C-type quartz veinlet. (c) L-type fluid inclusion in the B-type quartz veinlet. (d) Two-phase L-type fluid inclusions in the C-type veinlet. (e) V-type fluid inclusion in the A-type quartz veinlet. (f) Coexistence of V-type and L-type inclusions in the B-type quartz veinlet; V- and L-type fluid inclusions containing aqueous liquid and vapor. (g,h) Photomicrograph showing coexistence of S-type three-phase halite bearing and V-type two-phase fluid inclusions. (i) Three-phase fluid inclusion consists of liquid, vapor, opaque minerals in the A-type quartz veinlet. Abbreviations: L = liquid, V = vapor, H = halite, op = opaque mineral.

Quartz + tourmaline + pyrite  $\pm$  chalcopyrite veins or C-type veinlets have only L-type inclusions. The homogenization temperatures of L-type inclusion in the C-type veinlets were relatively lower than the inclusions in A- or B-type veinlets and range from 160 to 350 °C with 3.4–15.6 wt.% NaCl equivalent, respectively (Figure 11c).

#### 5.4. Whole-Rock Major and Trace Elements Composition

The SiO<sub>2</sub> contents of intrusive rocks at the Bayan-Uul deposit range from 54.7 wt.% to 69.1 wt.%. The LOI (loss of ignition) values of unaltered and least altered rocks range from 0.5 wt.% to 5.5 wt.%, while LOI values in altered rocks reach up to 12.5 wt.%. Based on whole rock geochemistry data and petrography analysis, intrusive rocks are classified into granodiorite, diorite porphyry, or monzodiorite. The TAS diagram for plutonic rocks using total alkalis (Na<sub>2</sub>O+K<sub>2</sub>O) versus SiO<sub>2</sub> diagram [36] illustrates that the intrusive rocks in the Bayan-Uul deposit are plotted as diorite, granodiorite, quartz-monzonite,

monzonite, and monzodiorite (Figure 12a). Further, the granitoids illustrated in the  $\text{SiO}_2$  versus  $\text{K}_2\text{O}$  discrimination diagram [37] clarify alkalinity. This indicates that rocks belong to the medium to high potassic calc-alkaline series in composition (Figure 12b).



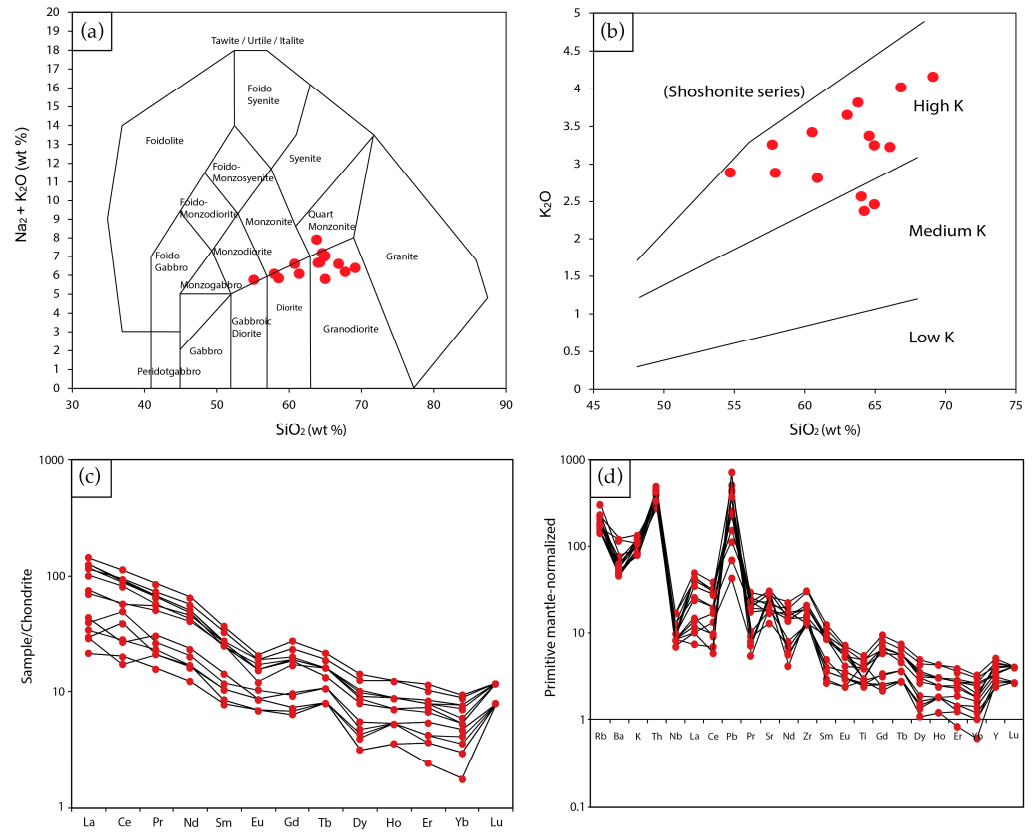
**Figure 11.** Histograms of homogenization temperature of fluid inclusions in different veinlets. (a) Fluid inclusions in A-type veinlet associated with phyllic and potassic alteration. (b) Fluid inclusions in B-type veinlet associated with potassic alteration. (c) Fluid inclusions in C-type veinlet associated with quartz–tourmaline–sericite alteration.

Table 1 provides concentration of the rare earth elements (REEs) and trace elements for intrusive rocks. Chondrite-normalized REE patterns [38] of all samples are enriched in light REEs and depleted in heavy REEs (Figure 12c). The Sr/Y ratio of intrusive rocks of the Bayan-Uul deposit ranges from 19.6 to 54.8. Regarding the REE composition  $(\text{La}/\text{Yb})_N$ , values in granodiorite, diorite porphyry, and monzodiorite range from 9.3 to 22.5, 7.2 to 15.6, and 15.2 to 17.5, respectively, the  $(\text{Gd}/\text{Yb})_N$  values of granodiorite, diorite porphyry, and monzodiorite range from 2.2 to 2.8, 1.9 to 3.6, and 2.4 to 4.2, respectively, and the  $(\text{Eu}/\text{Eu}^*)$  values range from 0.61 to 1, 0.66 to 0.99, and 0.67 to 0.84, respectively. The primitive mantle-normalized [38] trace elements diagram of intrusive rocks in the Bayan-Uul deposit shows enrichments of large ion lithophile elements (LILE), such as K, Th, Rb, Sr, and Pb, and depletion of high field strength elements (HFSE) such as Nb and Ti with no negative Zr anomalies (Figure 12d). The Bayan-Uul granitoids Mg# ranges from 14.13 to 30.22.

### 5.5. O-S Isotope Results

The oxygen and sulfur isotope analysis data are shown in (Table 2). A-type, B-type, and C-type quartz vein samples recorded  $\delta^{18}\text{O}$  values are 8.4‰, 10.9‰, and 8.7‰, respectively. The  $\delta^{18}\text{O}_{\text{H}_2\text{O}}$  values of ore-forming fluids are calculated using the equation of  $1000 \ln \alpha_{\text{quartz-H}_2\text{O}} = 3.38 \times 10^6 T^{-2} - 3.40$  [39], combined with the measured  $\delta^{18}\text{O}$  quartz values and the corresponding fluid inclusions homogenization temperatures of the quartz

samples in this study. The calculated  $\delta^{18}\text{O}_{\text{H}_2\text{O}}$  value in A-type, B-type, and C-type veins are 5.3‰, 7.8‰, and 5.6‰ respectively. The  $\delta^{34}\text{S}$  values of seven mineral separates of chalcopyrite, molybdenite, and pyrite in the Bayan-Uul deposit are summarized in Table 2. The overall S isotopic range is from  $-0.6\text{‰}$  to 5.3‰. The three chalcopyrite samples  $\delta^{34}\text{S}$  values are  $-0.5\text{‰}$ ,  $-0.6\text{‰}$ , and 2.3‰, whereas the three pyrite samples  $\delta^{34}\text{S}$  values are 5.3‰,  $-1.4\text{‰}$ , and 2.1‰. The  $\delta^{34}\text{S}$  value of molybdenite sample yielded 1.9‰.



**Figure 12.** (a) Geochemistry of the intrusive rocks on the classification diagram of intrusive rock according to total alkaline content and silica content [36]. (b) SiO<sub>2</sub> versus K<sub>2</sub>O (wt.%) diagram of [37]. (c) Chondrite-normalized spider diagram. (d) Primitive-mantle-normalized spider diagram. Normalization values are from [38].

**Table 1.** Chemical composition of host rocks from porphyry type mineralization zone.

Rock Type	Granodiorite							
Sample ID	BU180815-2	BDH78-2	BDH78-5	BDH78-27	BDH78-46	BDH78-47	BDH74	BDH78-45
SiO <sub>2</sub>	69.10	64.01	64.95	64.22	64.95	64.57	66.82	63.77
TiO <sub>2</sub>	0.55	0.86	0.87	0.57	0.63	0.64	0.53	0.62
Al <sub>2</sub> O <sub>3</sub>	14.16	14.46	12.50	13.63	14.82	14.63	13.89	14.57
FeO	2.99	3.61	4.27	2.89	3.86	4.04	2.45	3.80
MnO	0.05	0.02	0.02	0.01	0.06	0.06	0.02	0.04
MgO	2.03	4.93	6.13	4.10	3.53	3.62	2.84	3.30
CaO	3.38	2.51	2.51	3.01	4.09	3.99	2.95	4.22
Na <sub>2</sub> O	2.24	4.09	3.34	4.32	3.79	3.79	2.60	4.09
K <sub>2</sub> O	4.16	2.57	2.46	2.38	3.25	3.38	4.02	3.82
P <sub>2</sub> O <sub>5</sub>	0.55	0.29	0.30	0.19	0.22	0.23	0.15	0.21
LOI	0.52	2.34	2.09	3.45	0.58	0.69	2.54	1.34
S	0.01	0.12	0.36	1.08	0.01	0.08	0.79	0.04
Total (wt.%)	99.74	99.81	99.80	99.85	99.79	99.72	99.60	99.82

Table 1. Cont.

Rock Type	Granodiorite							
Cu (ppm)	9	150	224	174	11	718	1589	71
Zn	47	34	27	50	50	49	21	23
Pb	6	18	18	50	16	17	26	18
V	77	76	73	47	52	52	68	61
Cr	89	117	113	78	49	51	111	44
Co	22	38	36	16	35	35	30	26
Ni	68	52	58	35	35	36	60	35
As	53	33	64	16	23	25	7	16
Mo	22	12	238	9	9	163	19	22
Rb	147	93	111	91	106	113	141	146
Sr	605	387	359	562	647	619	603	275
Ba	768	328	215	380	458	443	847	397
Y	30	18	16	11	15	15	15	13
Zr	142	222	211	152	145	169	152	154
Nb	6	7	7	5	6	7	6	6
Th	38.4	41.8	36.2	27.4	38.3	36.5	28.0	25.1
Sc	8.4	9.4	7.7	6.0	9.2	8.8	4.1	4.0
La	26.1	16.4	29.6	6.9	29.7	23.9	8.1	9.4
Ce	37.5	35.2	55.1	10.4	55.7	49.1	17.2	29.9
Pr	15.7	4.8	6.3	2.0	6.2	5.4	2.1	2.5
Nd	24.2	18.9	23.3	7.6	23.3	19.6	7.8	9.4
Sm	n.d	3.90	4.0	1.6	4.1	3.8	1.6	1.7
Eu	n.d	0.75	0.8	0.4	1.0	1.0	0.5	0.6
Gd	n.d	3.48	3.8	1.4	4.1	3.8	1.5	1.8
Tb	n.d	0.55	0.5	0.3	0.5	0.5	0.3	0.3
Dy	n.d	2.33	2.2	1.0	2.6	2.4	1.1	1.2
Ho	n.d	0.51	0.4	0.2	0.5	0.5	0.2	0.2
Er	n.d	1.29	1.1	0.6	1.3	1.3	0.6	0.7
Tm	n.d	0.28	0.2	0.2	0.3	0.3	0.2	0.2
Yb	n.d	1.03	0.9	0.5	1.2	1.2	0.5	0.6
Lu	n.d	0.25	0.2	0.2	0.2	0.3	0.2	0.2
(La/Yb) <sub>N</sub>	n.d	11.5	22.4	9.3	17.5	13.6	10.0	9.7
(La/Sm) <sub>N</sub>	n.d	2.7	4.7	2.7	4.6	4.0	3.1	3.4
(Gd/Yb) <sub>N</sub>	n.d	2.8	3.3	2.2	2.8	2.5	2.1	2.2
Eu/Eu*	n.d	0.6	0.6	0.8	0.7	0.7	0.9	1.0
Rock type	Diorite porphyry				Monzodiorite			
Sample ID	BDH78-22	BDH78-26	BDH72	BDH82	BDH78-41	BDH78-8	BDH78-39	
SiO <sub>2</sub>	57.92	63.02	60.87	66.05	60.54	57.69	54.70	
TiO <sub>2</sub>	1.20	0.61	1.08	0.55	1.03	0.66	0.96	
Al <sub>2</sub> O <sub>3</sub>	13.81	14.29	15.07	14.62	14.13	13.47	11.76	
FeO	5.42	3.20	4.97	2.82	4.89	7.9	6.64	
MnO	0.08	0.01	0.01	0.01	0.07	0.02	0.03	
MgO	5.26	3.03	4.91	2.35	4.92	4.31	5.30	
CaO	5.62	3.11	1.99	2.53	3.97	1.92	5.89	
Na <sub>2</sub> O	2.96	3.35	3.20	3.01	3.06	2.69	2.81	
K <sub>2</sub> O	2.90	3.67	2.84	3.24	3.44	3.26	2.89	
P <sub>2</sub> O <sub>5</sub>	0.35	0.20	0.42	0.18	0.30	0.32	0.33	
LOI	4.25	4.34	3.32	3.82	3.42	4.4	5.54	
S	0.02	0.98	0.57	0.59	0.02	2.84	2.50	
Total (wt.%)	99.79	99.81	99.25	99.77	99.79	99.48	99.35	
Cu (ppm)	21	55	5134	60	24	2935	3356	
Zn	64	34	41	40	46	21	43	
Pb	8	31	5	30	11	36	3	
V	96	51	142	80	86	102	102	
Cr	63	48	140	91	43	130	294	
Co	37	45	52	30	27	47	53	
Ni	57	36	91	42	48	75	138	
As	23	24	7	31	15	137	9	
Mo	11	9	9	10	10	9	87	
Rb	89	118	190	102	109	117	131	
Sr	561	436	391	386	441	480	572	
Ba	320	500	544	822	331	439	339	
Y	23	13	20	14	19	21	12	
Zr	342	179	237	144	337	212	142	

Table 1. Cont.

Rock Type	Granodiorite						
Nb	12	6	9	6	12	9	6
Th	37.2	26.5	28.7	34.0	37.7	33.4	23.5
Sc	14.2	4.8	10.7	4.7	11.9	11.0	6.9
La	33.9	5.0	17.9	10.2	27.4	27.6	6.9
Ce	68.8	12.3	34.8	16.4	57.1	53.6	23.8
Pr	8.1	1.5	5.2	2.8	6.9	6.2	2.0
Nd	30.3	5.7	21.0	10.9	26.2	22.2	7.8
Sm	5.5	1.1	4.1	2.1	4.9	3.8	1.3
Eu	1.2	0.4	0.9	0.4	1.1	0.8	0.3
Gd	5.5	1.2	3.8	1.9	4.7	3.9	1.4
Tb	0.7	0.2	0.5	0.3	0.7	0.5	0.2
Dy	3.5	0.8	2.0	1.3	3.1	2.2	0.8
Ho	0.7	0.2	0.4	0.3	0.6	0.5	0.2
Er	1.9	0.6	1.1	0.8	1.7	1.4	0.4
Tm	0.4	0.2	0.2	0.2	0.3	0.3	0.1
Yb	1.5	0.5	0.8	0.8	1.5	1.3	0.2
Lu	0.3	0.2	0.2	0.2	0.3	0.3	0.1
(La/Yb) <sub>N</sub>	15.6	7.2	14.6	8.9	12.9	15.2	17.5
(La/Sm) <sub>N</sub>	3.9	2.7	2.8	3.0	3.5	4.6	3.3
(Gd/Yb) <sub>N</sub>	2.9	2.1	3.6	1.9	2.6	2.4	4.2
Eu/Eu*	0.6	0.9	0.6	0.6	0.6	0.6	0.8

Major (wt.%), minor (ppm), (n.d = not determined).

**Table 2.** Sulfur and oxygen isotope compositions of the sulfides and quartz from the Bayan-Uul Au-Cu-(Mo) porphyry deposit.

Sample No	Mineral	Occurrence	Vein Type	$\delta^{34}\text{S}_{\text{V-CDT}}(\text{‰})$	$\delta^{18}\text{O}_{\text{H}_2\text{O}}(\text{‰})$
BDH-42-1	Chalcopyrite	Disseminated	-	-0.5	-
BU180815-5	Chalcopyrite	Outcrop	-	-0.6	-
BU180815-6	Chalcopyrite	Disseminated with Au	-	2.3	-
BDH-78-36	Pyrite	qtz+tur+mo+cpy+py vein	B-type	5.3	-
BDH-78-14	Pyrite	qtz+tur+py±cpy vein	C-type	-1.4	-
BU180815-7	Molybdenite	Disseminated	-	1.9	-
BDH-78-1	Pyrite	qtz+tur+py±cpy vein	C-type	2.1	-
BDH-78-14	Quarz	Along fracture	C-type	-	5.6
BDH-78-36	Quarz	Along fracture	B-type	-	7.8
BDH-78-43	Quarz	Along fracture	A-type	-	5.3

Abbreviations: qtz = quartz, tur = tourmaline, py = pyrite, cpy = chalcopyrite, mol = molybdenite.

## 6. Discussions

Geological survey reports are the only sources of information regarding the petrogenesis and classification of the Bayan-Uul Au-Cu-(Mo) deposit. In addition, the mineralization, genesis, and ore-forming fluid environment studies have not been conducted. In this study, we aimed to (i) characterize the mineralization style at the Bayan-Uul deposit through a comparison litho-geochemical study of the Oyu-Tolgoi and Erdenet deposit's granitoid rocks that host the Au, Cu, and Mo mineralization; and (ii) to elucidate the ore-forming fluid environment that led to the formation and precipitation of the Bayan-Uul Au-Cu-(Mo) deposit. The formation environment can be applied as a criterion to further exploration of porphyry deposits in the similar geologic setting along the Central Mongolian and other areas in Mongolia.

### 6.1. Comparison with Other Porphyries

Geochemically, the Erdenet (giant) Cu-Mo deposit's porphyry-related suite is identified by a relatively high Sr/Y ratio ( $\text{Sr}/\text{Y} > 20$ ) and ( $\text{La}/\text{Yb} > 20$ ) with increasing  $\text{SiO}_2$  (Figure 13c). Meanwhile, Sr/Y and La/Yb ratios of the Oyu-Tolgoi (supergiant) porphyry Cu-Au deposit's intrusive rocks range from 19 to 60 and 6 to 26, respectively. In addition, Sr/Y and La/Yb ratios of the Bayan-Uul (moderate) Au-Cu-(Mo) deposit's porphyry-

related suite are identified as 19–50 and 10–33, respectively (Figure 13a,b). Magmatic fertility associated with porphyry-type mineralization system appear to have adakitic affinity, which is geochemically defined as  $Sr/Y > 20$ ,  $La/Yb > 20$ ,  $Sr > 400$  ppm,  $Y < 18$  ppm, and  $Yb < 1.9$  ppm, caused by residual and/or fractional crystallization of the minerals garnet, hornblende, and titanite [40,41]. The low to moderate  $Sr/Y$  and ( $La/Yb < 20$ ) ratios of Oyu-Tolgoi and Bayan-Uul does not fall within the adakitic field (Figure 13). However, adakitic magmas do not necessarily form porphyry type mineralization and the origin of high  $Sr/Y$  signatures (i.e., adakitic signatures) in magma is still actively debated. In addition,  $Sr/Y$  values of magmatic rocks associated with porphyry Cu-Au deposits demonstrate that Cu-rich porphyry Cu-Au deposits are associated with intrusions that have an average  $Sr/Y$  of  $100 \pm 50$ , whereas Au-rich porphyry Cu-Au deposits are associated with magmatic rocks that have a lower average  $Sr/Y$  value of  $50 \pm 25$  [42,43]. Therefore, the Bayan-Uul deposit porphyry-related suite illustrates signs of gold-rich porphyry.

As a well-known geochemical signature for porphyry Cu deposits [41], the chondrite-normalized REE pattern (Figure 12c) of the mineralized intrusion at Bayan-Uul shows moderate fractionation reflected in  $(La/Yb)_N = 7.2\text{--}22.5$  and a lack of Eu anomaly ( $Eu/Eu^* = 0.61\text{--}1$ ). These findings suggest porphyry-related oxidized and hydrous magma. Additionally, in contrast to barren earlier volcano-plutonic rocks in an immature arc, the flat-to-concave upward MREE–HREE pattern (Figure 12c) and  $(La/Sm)_N = 2.73\text{--}4.72$  and  $(Dy/Yb)_N = 1.08\text{--}1.84$  serves as geochemical characteristics of a porphyry-related intrusive suite that develops as an island arc matures. These geochemical signatures have been reported for porphyry Cu deposits worldwide, including those developed in association with the Tethyan arc magmatism [41], Oyu-Tolgoi [44], and Erdenet [45]. The hydrous nature of the magma, another precursor for fertile magma in magmatic arc systems [46], is also reflected by the hydrous mineral assemblages, i.e., abundant hornblende and biotite (Figure 6). In addition, the REE pattern of the intrusive rocks is characterized by enrichment of LREE and depletion of HREE (Figure 12c). Moreover, the enrichment of LILEs or subduction-related mobile elements such as K, Th, Rb, Sr, and Pb and the depletion of Nb and Ti anomalies are the main character of a subduction-related tectonic setting (Figure 12d); [47]. In the Y versus Nb and Rb versus Nb+Yb diagrams (Figure 13e,f); Ref. [48] the samples plot within the field of volcanic arc granite. With the island arc developing toward maturity, water, sulfur, and fluid-mobile components from the subducting oceanic slab enter the mantle wedge, causing it to become progressively more hydrated and oxidized [49]. This process has been estimated to last over  $\sim 10$  Ma from the nascent island arc stage [50,51].

The Mg# value indicates whether the source of magma that created the rock was originated solely from crustal material or from crustal material contaminated by mantle material [52]. Melts from the basaltic lower crust, in general, have a low Mg#  $< 40$ , regardless of melting degree. The Bayan-Uul granitoids with Mg# ranging from 14.13 to 30.22 are indicative of lower crust source.

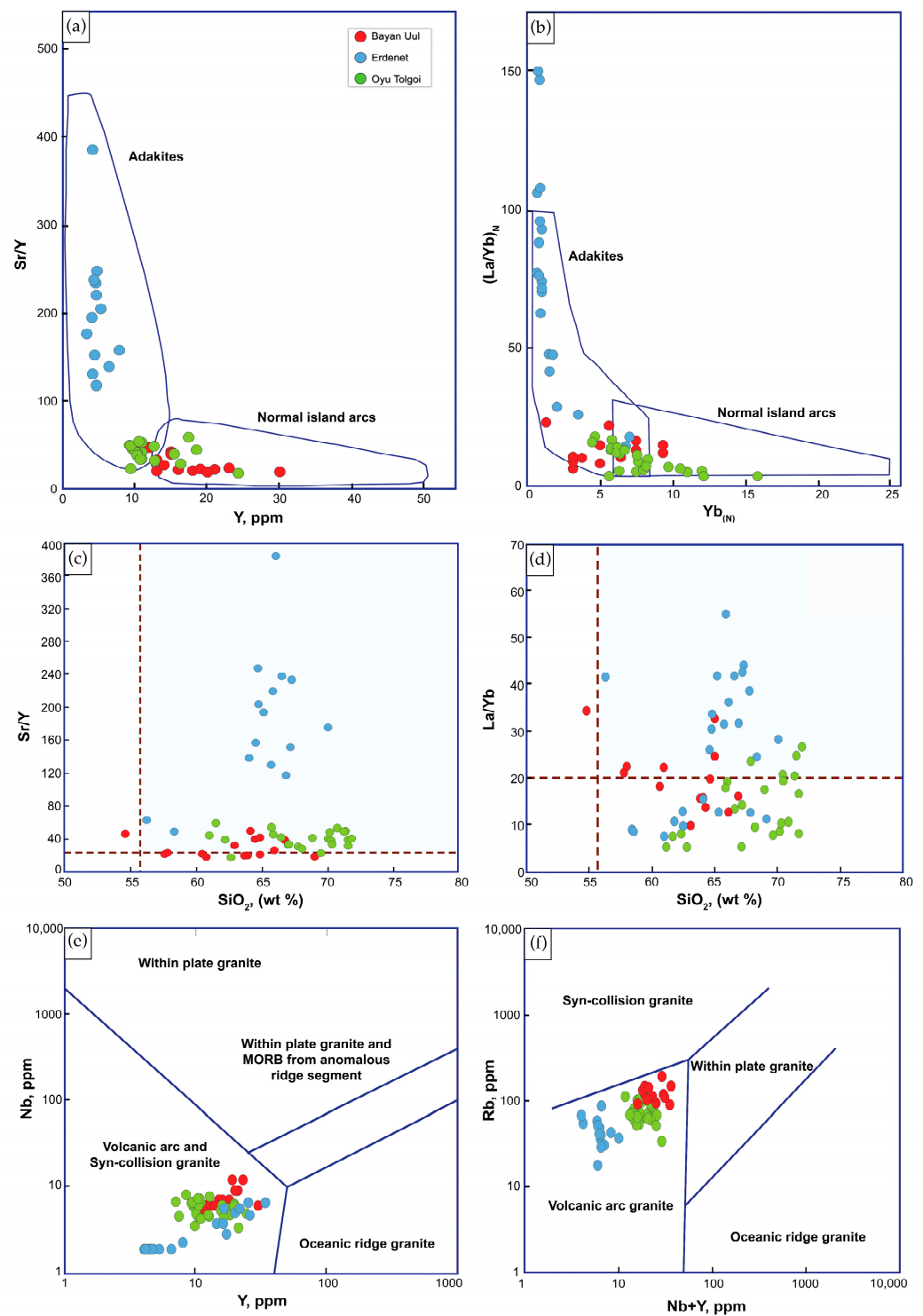


**Figure 13.** (a) Sr/Y versus Y ppm diagram with fields. (b)  $(La/Yb)_N$  versus  $Yb_N$  diagram with fields from [53]. (c) Sr/Y versus  $SiO_2$  plot show magma fertility after [42]. (d) La/Yb versus  $SiO_2$  diagram from [54] and (e) Nb versus Y. (f) Rb versus Y+Nb diagram for the tectonic discrimination of plutonic rocks [48].

### 6.2. Nature of Ore-Forming Fluids and Metal Source

Fluid inclusions preserve the history of ore-forming fluid systems and shed light on the characteristics and origins of the fluids [55–57]. The initial fluids that are exsolved from felsic magmas have a salinity of low to moderate, with 2 to 12% NaCl equivalent [58,59].

Melts appear to be more enriched in H<sub>2</sub>O, S, and Cl rather than in metals, especially Cu, suggesting that the source mechanisms leading to the development of primitive arc basalts, the ultimate parents of more advanced intermediate to felsic magmas associated with porphyry deposits, are more significant [60]. Hence, for Cu–Au porphyry deposits, chloride (Cl<sup>−</sup>) is likely to be the dominant ligand for Cu and Au, explaining their close association in this environment [61]. In addition, The Cl<sup>−</sup> ligand predicted the strong partitioning of both Cu and Au into high-temperature, oxidizing, high-salinity hydrothermal fluids [62]. Therefore, the moderate to high salinity of solutions of the Bayan-Uul porphyry deposit suggests that the ore compositions were transported by a chloride ligand. Moreover, the NaCl-dominated ore-bearing fluid is a typical characteristic of porphyry deposits [63]. A significant portion of the magma's CO<sub>2</sub> will have been lost by the time it reaches the mid-upper crust and evolves into more felsic compositions and exsolved fluids will be primarily hydrous and contain high concentrations of S-Cl [64]. Increasing S and Cl concentration with low pH conditions aided Cu and Au solubility and caused phyllic alteration. Therefore, Bayan-Uul deposits are dominated by phyllic alteration, and the biotite and other minerals of the host rocks are observed to be replaced by chlorite.

Once ascending from their igneous source, such fluids usually separate into a hypersaline liquid and a low salinity vapor phase during decompression and boiling. Selected sulfide mineralized quartz veinlets of the Bayan-Uul deposit show coexisting of primary L-type, V-type, and S-type halite bearing inclusions in A-type and B-type veinlets (Figure 10g,h) with similar homogenization temperatures but contrasting salinities of these fluid inclusions (Figure 14) support the fluid boiling evidence. Boiling can cause ore deposition [65] and also a separation of the hydrothermal system [63]. Shallow fluid boiling also aided in the entry of ore-metal into veins by promoting hydrofracturing and the development of a network of faults and fractures inside the granitoid [65]. Therefore, boiling was possibly the main mechanism for ore formation at the Bayan-Uul porphyry deposit.

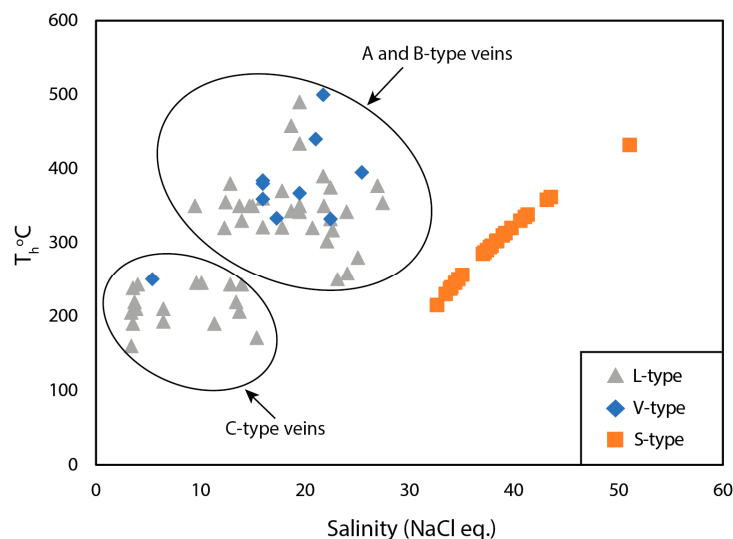


**Figure 14.** Homogenization temperature  $T_h$  °C versus salinity NaCl (wt.%) plot for different types of fluid inclusion data from the Bayan-Uul porphyry Au-Cu-(Mo) deposit. V-type = Vapor-rich two-phase FIs, L-type = Liquid-rich two-phase FIs, S-type = Solid-bearing three-phase FIs.

The polyphase hypersaline inclusions homogenize in two ways: vapor phase disappearance temperature higher than halite dissolution temperature, observed rarely ( $T_h > T_d$ ), or most of the polyphase inclusions are noted with vapor disappearance temperature lower than halite dissolution temperature ( $T_h < T_d$ ). Where  $T_h < T_d$ , results indicate the hydrothermal solution was saturated with NaCl at the trapping temperature. Similar phenomena have been reported from several porphyry deposits such as the Mamut deposit in Malaysia [66], the Dizon deposit in the Philippines [67], and the Batu Hijau deposit in

Indonesia [68,69]. Thus, the minimum homogenization temperature (around 220 °C) of halite-bearing polyphase inclusion can be considered as trapping temperature. In addition, the trapping temperatures of L-type two-phase fluid inclusions in A-, B-, and C-type quartz veinlets are considered (around 220 °C, 280 °C, and 160 °C).

On Earth, there are three key reservoirs containing different sulfur isotope compositions: (a) mantle or magmatic sulfur ( $0\% \pm 3\%$ ); (b) seawater sulfate ( $+20\%$ ); and (c) reduced sulfur or biogenic sulfur in sedimentary rocks (less than  $0\%$ ) [70]. For the majority of porphyry Cu-Mo and Mo deposits worldwide, the  $\delta^{34}\text{S}$  values of sulfide minerals generally vary from  $-5\%$  to  $+5\%$  [71]. Our new result shows that the  $\delta^{34}\text{S}$  values of the sulfide from the Bayan-Uul Au-Cu-(Mo) porphyry deposit exhibit  $-0.5\%$  to  $5.3\%$  (Figure 15a). Except in very small excess of the  $\delta^{34}\text{S}$  values of sulfide ( $5.3\%$ ) coincide closely with the sulfur isotopic data distribution for sulfide minerals found in the majority of porphyry deposits. The  $\delta^{18}\text{O}$  values of ore fluids from different mineralizing A-, B-, and C-type veins are  $8.7\%$ ,  $10.9\%$ , and  $8.4\%$ , respectively (Figure 15b). The hydrothermal quartz in A-, B-, and C-type veins from the Bayan-Uul Au-Cu-(Mo) deposit illustrate highly clustered  $\delta^{18}\text{O}_{\text{H}_2\text{O}}$  values of  $5.3\%$ ,  $7.8\%$ , and  $5.6\%$ , similar to primary magmatic water [72], indicative of a single magmatic origin rather than multiple sources of oxygen.

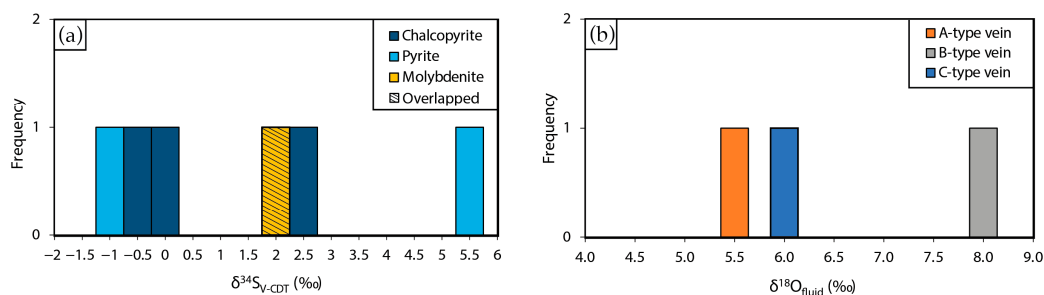


**Figure 15.** Histograms of (a)  $\delta^{34}\text{S}_{\text{V-CDT}}$  (‰) isotope composition of sulfides and (b)  $\delta^{18}\text{O}_{\text{fluid}}$  (‰) isotope composition of quartz samples from the Bayan-Uul porphyry Au-Cu-(Mo) deposit.

## 7. Conclusions

The Bayan-Uul porphyry deposit is hosted mainly by Late Triassic–Early Jurassic high-K calc alkaline intrusive rocks, namely granodiorite, diorite porphyry, and monzodiorite. In addition, tourmaline breccia is also an important host rock which contains more high-grade copper than other host rocks.

According to the tectonic geochemical discrimination diagrams, they tend to be formed in subduction-related island-arc geodynamic setting, which is subduction evidence of the Mongol–Okhotsk Orogenic Belt. Low to moderate values of Sr/Y ranging from 19.5 to 51.1, moderate Y concentration ranging from 11 to 30 ppm,  $(\text{La}/\text{Yb})_{\text{N}}$  ranging from 7 to 23, and values of  $\text{Yb}_{\text{N}}$  ranging from 3.4 to 9.2 are consistent with auriferous porphyry deposits.

The stockwork, breccia, and vein type mineralization are recognized in the Bayan-Uul deposit. Three different types of mineralized veinlets were identified. A-type veinlets consist of quartz + tourmaline + chalcopyrite + magnetite + pyrite and infrequently electrum, B-type veinlets consist of quartz + tourmaline + molybdenum + chalcopyrite + pyrite, and C-type veinlets are characterized by quartz + tourmaline + pyrite with minor chalcopyrite.

The homogenization temperatures for the fluid inclusions in A-type, B-type, and C-type veinlets range from 215 to 490 °C, 215 to 550 °C, and 160 to 350 °C and their salinity varies from 5.4 to 43.5 wt.%, 16.0 to 51.1 wt.%, and 3.4 to 15.6 wt.% NaCl equivalent, respectively. High temperature and high salinity fluids likely originated from magma.

The moderate to high salinity of solutions of the Bayan-Uul deposit suggests that the ore compositions were transported in a dominant chloride ligand. The coexisting of primary L-type, V-type, and S-type halite-bearing inclusions in A-type and B-type veinlets, and the coexistence of similar homogenization temperatures and very different salinity inclusions, suggest boiling conditions.

The  $\delta^{18}\text{O}$  values of ore fluids from different mineralizing A-, B-, and C-type veins are 8.7‰, 10.9‰, and 8.4‰, respectively. Therefore, the Bayan-Uul Au-Cu-(Mo) deposit illustrates a magmatic origin.

**Author Contributions:** Conceptualization, B.-E.B.; methodology, J.S.; software, J.S.; validation, K.Y.; formal analysis, B.-E.B.; investigation, B.-E.B.; resources, O.S. and B.B.; data curation, J.S.; writing—original draft preparation, B.-E.B.; writing—review and editing, K.Y. and J.S.; visualization, B.-E.B.; supervision, K.Y. All authors have read and agreed to the published version of the manuscript.

**Funding:** This research was funded by the MJEED scholarship program, Center for Research for Innovation in Technology Minerals of MUST, Economic Geology Laboratory of Kyushu University.

**Data Availability Statement:** Data is contained within the article.

**Acknowledgments:** The first author greatly thanks Bolorchimeg Nanzad Tunnell of EMRGe Research Center, Missouri University of Science and Technology for providing a review and editing; Akira Imai and Thomas Tindell of Kyushu University for their support and editing. In addition, the authors greatly thank the MJEED scholarship program for the research funding. Millennium Storm LLC also provided support in the field work and resources.

**Conflicts of Interest:** Baasanjargal Borshigo is an employee of Millennium Storm LLC. The paper reflects the views of the scientists and not the company.

## References

- Sillitoe, R.H. Porphyry copper systems. *Econ. Geol.* **2010**, *105*, 3–41. [\[CrossRef\]](#)
- Richards, J.P. Tectonomagmatic precursors for porphyry Cu-(Mo-Au) deposit formation. *Econ. Geol.* **2003**, *98*, 1515–1533. [\[CrossRef\]](#)
- Chiaradia, M. Supergiant porphyry copper deposits are failed large eruptions. *Commun. Earth Environ.* **2022**, *3*, 107. [\[CrossRef\]](#)
- Batgerel, O.; Tsedendamba, O.; Amarzaya, K.; Battumur, D.; Lkhagvasuren, B. *Erdenetin Ovoo Cu-Mo Porphyry Deposit's Resource Report in 2021*; Erdenet SOE: Ulaanbaatar, Mongolia, 2021; (unpublished report In Mongolian)
- Koval, P.V.; Gotovsuren, A.; Ariunbileg, S.; Libatorov, Y.I. On Prospecting for Porphyry Copper Mineralization in Intracontinental Mobile Zones (Mongol-Okhotsk Belt, Mongolian People's Republic). *J. Geochem. Explor.* **1989**, *32*, 369–380. [\[CrossRef\]](#)
- Ariunbileg, S.; Hosbayar, P. Geochemical features of porphyry copper mineralization in the Bayan-Uul occurrence (Central Mongolia). *Mong. Geosci.* **1998**, *8*, 24–33.
- Lamb, M.A.; Cox, D. New  $40\text{Ar}/39\text{Ar}$  age data and implications for porphyry copper deposits of Mongolia. *Econ. Geol.* **1998**, *93*, 524–529. [\[CrossRef\]](#)
- Jargalan, S.; Dejidmaa, G.; Gantsetseg, O.; Ariunbileg, S.; Khurelbaatar, B.; Tsatsral, U.; Gurbadam, E. *Report on Metallogenic Map of Metallic Mineral Resources Mongolia at Scale 1:1000000 in 2021*; Department of Geology and Hydrogeology, Mongolian University Science and Technology: Ulaanbaatar, Mongolia, 2021; (unpublished report In Mongolian)
- Bussien, D.; Gombojav, N.; Winkler, W.; Quadt, A. The Mongol-Okhotsk Belt in Mongolia—An appraisal of the geodynamic development by the study of sandstone provenance and detrital zircons. *Tectonophysics* **2011**, *510*, 132–150. [\[CrossRef\]](#)
- Kurihara, T.; Tsukada, K.; Otoh, S.; Kashiwagi, K.; Chuluun, M.; Byambadash, D.; Boijir, B.; Gonchigdorj, S.; Nuramkhan, M.; Niwa, M.; et al. Upper Silurian and Devonian pelagic deep-water radiolarian chert from the Khangai-Khentei belt of Central Mongolia: Evidence for Middle Paleozoic subduction accretion activity in the Central Asian Orogenic Belt. *J. Asian Earth Sci.* **2009**, *34*, 209–225. [\[CrossRef\]](#)
- Badarch, G.; Cunningham, W.D.; Windley, B.F. A new terrane subdivision for Mongolia: Implications for the Phanerozoic crustal growth of Central Asia. *J. Asian Earth Sci.* **2002**, *21*, 87–110. [\[CrossRef\]](#)
- Donskaya, T.V.; Gladkochub, D.P.; Mazukabzov, A.M.; Ivanov, A.V. Late Paleozoic–Mesozoic subduction-related magmatism at the southern margin of the Siberian continent and the 150 million-year history of the Mongol-Okhotsk Ocean. *J. Asian Earth Sci.* **2013**, *62*, 79–97. [\[CrossRef\]](#)
- Zorin, Y.A.; Belichenko, V.G.; Turutanov, E.K.; Mazukabzov, A.M.; Sklyarov, E.V.; Mordvinova, V.V. The East Siberia Transect. *Int. Geol. Rev.* **1995**, *37*, 154–175. [\[CrossRef\]](#)
- Van der Voo, R.; van Hinsbergen, D.J.J.; Domeier, M.; Spakman, W.; Torsvik, T.H. Latest Jurassic—Earliest Cretaceous closure of the Mongol-Okhotsk Ocean: A paleomagnetic and seismological-tomographic analysis. In *Late Jurassic Margin of Laurasia—A record of Faulting Accommodating Plate Rotation*; Geological Society of America Special Paper; Anderson, T.H., Didenko, A.N., Johnson, C.L., Khanchuk, A.I., MacDonald, J.H., Eds.; The Geological Society of America: Boulder, CO, USA, 2015; Volume 513, pp. 589–606.
- Sorokin, A.A.; Zaika, V.A.; Kovach, V.P.; Kotov, A.B.; Xu, W.; Yang, H. Timing of closure of the eastern Mongol-Okhotsk Ocean: Constraints from U–Pb and Hf isotopic data of detrital zircons from metasediments along the Dzhagdy Transect. *Gondwana Res.* **2020**, *81*, 58–78. [\[CrossRef\]](#)

16. Yi, Z.; Meert, J.G. A closure of the Mongol–Okhotsk Ocean by the Middle Jurassic: Reconciliation of paleomagnetic and geological evidence. *Geophys. Res. Lett.* **2020**, *47*, 1–9. [[CrossRef](#)]
17. Tang, J.; Xu, W.L.; Feng, W.; Wei, W.; Mei-Jun, X.; Yi-Han, Z. Geochronology and geochemistry of Early–Middle Triassic magmatism in the Erguna Massif, NE China: Constraints on the tectonic evolution of the Mongol–Okhotsk Ocean. *Lithos* **2014**, *184–187*, 1–16. [[CrossRef](#)]
18. Zhao, P.; Xu, B.; Jahn, B.M. The Mongol–Okhotsk Ocean subduction-related Permian peraluminous granites in northeastern Mongolia: Constraints from zircon U–Pb ages, whole-rock elemental and Sr–Nd–Hf isotopic compositions. *J. Asian Earth Sci.* **2017**, *144*, 225–242. [[CrossRef](#)]
19. Li, Y.; Xu, W.L.; Wang, F.; Tang, J.; Zhao, S.; Guo, P. Geochronology and geochemistry of late Paleozoic–early Mesozoic igneous rocks of the Erguna Massif, NE China: Implications for the early evolution of the Mongol–Okhotsk tectonic regime. *J. Asian Earth Sci.* **2017**, *144*, 205–224. [[CrossRef](#)]
20. Kotov, A.; Larin, A.; Salnikova, E.; Velikoslavinskii, S.; Sorokin, A.; Yakovleva, S.; Anisimova, I.; Tolmacheva, E. Tok–Algoma magmatic complex of the Selenga–Stanovoi Superterrains in the Central Asian fold belt: Age and tectonic setting. *Dokl. Earth Sci.* **2012**, *444*, 562–567. [[CrossRef](#)]
21. Tsukada, K.; Nuramkhan, M.; Purevsuren, N.; Kabashima, T.; Kondo, T.; Gantumur, O.; Hasegawa, H.; Yamamoto, K. Permian adakitic magmatism in the Khanui Group, Northern Mongolia—Late Paleozoic slab-melting of subducted oceanic plate beneath the “Siberian continent”. *J. Geodyn.* **2018**, *121*, 49–63. [[CrossRef](#)]
22. Sun, D.Y.; Gou, J.; Wang, T.H.; Ren, Y.S.; Liu, Y.J.; Guo, H.Y.; Liu, X.M.; Hu, Z.C. Geochronological and geochemical constraints on the Erguna massif basement, NE China—subduction history of the Mongol–Okhotsk oceanic crust. *Int. Geol. Rev.* **2013**, *55*, 1801–1816. [[CrossRef](#)]
23. Tang, J.; Xu, W.L.; Wang, F.; Zhao, S.; Wang, W. Early Mesozoic southward subduction history of the Mongol–Okhotsk oceanic plate: Evidence from geochronology and geochemistry of Early Mesozoic intrusive rocks in the Erguna Massif, NE China. *Gondwana Res.* **2016**, *31*, 218–240. [[CrossRef](#)]
24. Ganbat, A.; Tsujimori, T.; Miao, L.; Safonova, I.; Pastor-Galán, D.; Anaad, C.; Munkhsengel, B.; Aoki, S.; Aoki, K.; Savinskiy, I. Late Paleozoic–Early Mesozoic granitoids in the Khangay–Khentey basin, Central Mongolia: Implication for the tectonic evolution of the Mongol–Okhotsk Ocean margin. *Lithos* **2021**, *404–405*, 106455. [[CrossRef](#)]
25. Zhu, M.; Miao, L.; Zhang, F.; Ganbat, A.; Baatar, M.; Anaad, C.; Yang, S.; Wang, Z. Carboniferous magmatic records of central Mongolia and its implications for the southward subduction of the Mongol–Okhotsk Ocean. *Int. Geol. Rev.* **2022**, *65*, 1–20. [[CrossRef](#)]
26. Yarmolyuk, V.V.; Kovalenko, V.I.; Sal’nikova, E.B.; Budnikov, S.V.; Kovach, V.P.; Kotov, A.B.; Ponomarchuk, V.A. Tectono-magmatic zoning, magma sources, and geodynamics of the Early Mesozoic Mongolia–Transbaikalian province. *Geotectonics* **2002**, *36*, 293–311.
27. Dolgov, G.A.; Bat-Erdene, D. *Research–Geophysical Complex Expedition and at Scale of 1:50,000 Geological Mapping, General Exploration Work and at Scale of 1:10,000 Detailed Exploration Work in 1984*; Geological Science Academy of the Russian Federation: Ulaanbaatar, Mongolia, 1984; (unpublished report In Mongolian)
28. Dejidmaa, G. *UGZ-200 Research Report in 2007*; Department of Minerals and Petroleum, an Implementing Agency of the Mongolian Government: Ulaanbaatar, Mongolia, 2007; (unpublished report In Mongolian)
29. Chuluun, O.; Baasanjargal, B.; Tsogtmagnai, B.; Ochirsuh, L. *Report on Geological Mapping at Scale of 1:2000 in the Area of Bayan-Uul between 2013–2014*; Millennium Storm LLC: Ulaanbaatar, Mongolia, 2014; (unpublished report In Mongolian)
30. Tseren-Ochir, S.; Terebenin, B.M.; Gansukh, M. *Report on Geological Mapping at Scale of 1:200,000 and Exploration Work in 1971*; Bayankhongor Geology Administration: Ulaanbaatar, Mongolia, 1971; (unpublished report In Mongolian)
31. Jargalsaikhan, D.; Baasanjargal, B. *Report on Geological Mapping at Scale of 1:20,000, Electrical and Magnetic Exploration and Drilling of Exploratory Wells in Bayan-Uul Area in 2010*; “Universal Minerals” LLC: Ulaanbaatar, Mongolia, 2010; (unpublished report In Mongolian)
32. Bodnar, R.J.; Reynolds, T.J.; Kuehn, C.A. Fluid-inclusions systematics in epithermal systems. In *Geology and Geochemistry of Epithermal Systems*; Reviews in Economic Geology; Berger, B.R., Bthke, P.M., Eds.; Society of Economic Geologists: Littleton, CO, USA, 1985; Volume 2, pp. 73–97.
33. Sterner, S.M.; Hall, D.L.; Bodnar, R.J. Synthetic fluid inclusions. V. Solubility relations in the system NaCl–KCl–H<sub>2</sub>O under vapor saturated conditions. *Geochim. Cosmochim. Acta* **1988**, *52*, 989–1005. [[CrossRef](#)]
34. Clayton, R.N.; Mayeda, T.K.; Goswami, J.N.; Olsen, E.J. Oxygen isotope studies of ordinary chondrites. *Geochim. Cosmochim. Acta* **1991**, *55*, 2317–2337. [[CrossRef](#)]
35. Gustafson, L.B.; Hunt, J.P. The porphyry copper deposit at El Salvador, Chile. *Econ. Geol.* **1975**, *70*, 857–912. [[CrossRef](#)]
36. Middlemost, E.A.K. Naming materials in magma/igneous rock system. *Earth Sci. Rev.* **1994**, *37*, 215–224. [[CrossRef](#)]
37. Peccerillo, A.; Taylor, S.R. Geochemistry of Eocene Cal–Alkaline Volcanic Rocks from Kastamonu Area, Northern Turkey. *Contrib. Mineral. Petrol.* **1976**, *25*, 68–81.
38. McDonough, W.; Sun, S. The composition of the Earth. *Chem. Geol.* **1995**, *120*, 223–253. [[CrossRef](#)]
39. Clayton, R.N.; O’Neil, J.R.; Mayeda, T.K. Oxygen isotope exchange between quartz and water. *J. Geophys. Res.* **1972**, *77*, 3057–3067. [[CrossRef](#)]
40. Richards, J.P.; Kerrich, R. Special Paper: Adakite-like rocks: Their diverse origins and questionable role in metallogenesis. *Econ. Geol.* **2007**, *102*, 537–576. [[CrossRef](#)]

41. Richards, J.P.; Spell, T.; Rameh, E.; Razique, A.; Fletcher, T. High Sr/Y magmas reflect arc maturity, high magmatic water content, and porphyry Cu ± Mo ± Au potential: Examples from the Tethyan Arcs of Central and Eastern Iran and Western Pakistan. *Econ. Geol.* **2012**, *107*, 295–332. [[CrossRef](#)]
42. Loucks, R.R. Distinctive composition of copper-ore-forming arc magmas. *Aust. J. Earth Sci.* **2014**, *61*, 5–16. [[CrossRef](#)]
43. Chiaradia, M. Distinct magma evolution processes control the formation of porphyry Cu–Au deposits in thin and thick arcs. *Earth Planet. Sci. Lett.* **2022**, *599*, 117864. [[CrossRef](#)]
44. Crane, D.; Kavalieris, I. Geologic overview of the Oyu Tolgoi porphyry Cu–Au–Mo deposits, Mongolia. In *Geology and Genesis of Major Copper Deposits and Districts of the World: A Tribute to Sillitoe, R. H.*; Hedenquist, J.W., Harris, M., Camus, F., Eds.; Special Publication; Society of Economic Geologists: Littleton, CO, USA, 2012; Volume 16, pp. 187–213.
45. Kavalieris, I.; Khashgerel, B.-E.; Morgan, L.E.; Undrakhtamir, A.; Borohul, A. Characteristics and <sup>40</sup>Ar/<sup>39</sup>Ar geochronology of the Erdenet Cu–Mo deposit, Mongolia. *Econ. Geol.* **2017**, *112*, 1033–1053. [[CrossRef](#)]
46. Richards, J.P. High Sr/Y arc magmas and porphyry Cu ± Mo ± Au deposits: Just add water. *Econ. Geol.* **2011**, *106*, 1075–1081. [[CrossRef](#)]
47. Wood, D.A.; Jordan, J.L.; Treuil, M. A re-appraisal of the use of trace elements to classify and discriminate between magma series erupted in different tectonic settings. *Earth Planet. Sci. Lett.* **1979**, *45*, 326–336. [[CrossRef](#)]
48. Pearce, J.A.; Harris, N.B.W.; Tindle, A.G. Trace element discrimination diagrams for the tectonic interpretation of granite rocks. *J. Petrol.* **1984**, *25*, 956–983. [[CrossRef](#)]
49. Enkhjargal, B.; Bolorchimeg, N.; Jargalan, S.; Marek, L.; Yasuhito, O.; Navchaa, B.; Khashbat, D.; Ariunbat, Z. Geochronology and geochemistry of the intrusive suite associated with the Khatsavch porphyry Cu–Au (Mo) deposit, South Mongolia. *Ore Geol. Rev.* **2019**, *111*, 102978.
50. Evans, K.A.; Elburg, M.A.; Kamenetsky, V.S. Oxidation state of subarc mantle. *Geology* **2012**, *40*, 783–786. [[CrossRef](#)]
51. Richards, J.P. The oxidation state, and sulfur and Cu contents of arc magmas: Implications for metallogeny. *Lithos* **2015**, *233*, 27–45. [[CrossRef](#)]
52. Smithies, R.; Champion, D. The Archaean High-Mg Diorite Suite: Links to Tonalite-Trondhjemite-Granodiorite Magmatism and Implications for Early Archaean Crustal Growth. *J. Petrol.* **2000**, *41*, 1653–1671. [[CrossRef](#)]
53. Defant, M.J.; Drummond, M.S. Derivation of some modern arc magmas by melting of young subducted lithosphere. *Nature* **1990**, *347*, 662–665. [[CrossRef](#)]
54. Davidson, J.; Turner, S.; Handley, H.; Macpherson, C.; Dosseto, A. Amphibole “sponge” in arc crust? *Geology* **2007**, *35*, 787–790. [[CrossRef](#)]
55. Roedder, E. Fluid inclusions. In *Reviews in Mineralogy*; Mineralogical Society of America: Chantilly, VA, USA, 1984; Volume 12, pp. 1–644.
56. Ulrich, T.; Guenther, D.; Heinrich, C.A. Gold concentrations of magmatic brines and the metal budget of porphyry copper deposits. *Nature* **1999**, *399*, 676–679. [[CrossRef](#)]
57. Pirajno, F. *Hydrothermal Processes and Mineral Systems*; Springer: Berlin/Heidelberg, Germany, 2009; p. 1250.
58. Redmond, P.B.; Einaudi, M.T.; Inan, E.E. Copper deposition by fluid cooling in intrusion-centered systems: New insights from the Bingham porphyry ore deposit, Utah. *Geology* **2004**, *32*, 217–220. [[CrossRef](#)]
59. Rusk, B.G.; Reed, M.H.; Dilles, J.H.; Klemm, L.M.; Heinrich, C.A. Compositions of magmatic hydrothermal fluids determined by LA–ICP–MS of fluid inclusions from the porphyry copper–molybdenum deposit at Butte, MT. *Chem. Geol.* **2004**, *210*, 173–199. [[CrossRef](#)]
60. Chiaradia, M. Magmatic Controls on Metal Endowment of Porphyry Cu–Au Deposits. In *Tectonomagmatic Influences on Metallogeny and Hydrothermal Ore Deposit: A Tribute to Jeremy P.R.*; Sholeh, A., Wang, R., Eds.; Society of Economic Geologists: Littleton, CO, USA, 2021; Volume I, pp. 1–16.
61. Vearncombe, J.R. Function and status of structural geology in the Resource industry. *Aust. J. Earth Sci.* **2023**, *70*, 908–931. [[CrossRef](#)]
62. Puddephatt, R.J. *The Chemistry of Gold*; Elsevier: Amsterdam, The Netherlands, 1978.
63. Heinrich, C.A.; Günther, D.; Audétat, A.; Ulrich, T.; Frischnecht, R. Metal fraction between magmatic brine and vapor, determined by microanalysis of fluid inclusions. *Geology* **1999**, *27*, 755–758. [[CrossRef](#)]
64. Richards, J.P. Porphyry copper deposit formation in arcs: What are the odds? *Geosphere* **2021**, *18*, 130–155. [[CrossRef](#)]
65. Hedenquist, J.W.; Arribas, A.J.; Reynolds, T.J. Evolution of an intrusion-centered hydrothermal system: Far Southeast-Lepanto porphyry and epithermal Cu–Au deposits, Philippines. *Econ. Geol.* **1998**, *93*, 373–404. [[CrossRef](#)]
66. Imai, A. Genesis of the Mamut porphyry copper deposit, Sabah, East Malaysia. *Resour. Geol.* **2000**, *50*, 1–23. [[CrossRef](#)]
67. Imai, A. Evolution of hydrothermal system at the Dizon porphyry Cu–Au deposit, Zambales, Philippines. *Resour. Geol.* **2005**, *55*, 73–90. [[CrossRef](#)]
68. Imai, A.; Ohno, S. Primary ore mineral assemblage and Fluid inclusion study of the Batu Hijau porphyry Cu–Au deposit, Suwabawa, Indonesia. *Resour. Geol.* **2005**, *55*, 239–248. [[CrossRef](#)]
69. Imai, A.; Nagai, Y. Fluid inclusion Study and Opaque Mineral Assemblage at the Deep and Shallow Part of the Batu Hijau Porphyry Copper–gold Deposit, Sumbawa, Indonesia. *Resour. Geol.* **2009**, *59*, 231–243. [[CrossRef](#)]
70. Hoefs, D.J. Geochemistry of Stable Isotopes. *Angew. Chem. Int. Ed.* **1975**, *14*, 75–79. [[CrossRef](#)]

71. Fang, F.Z.; Yin, H.W.; Jia, J.L.; Jian, P.W.; Chun, B.Z.; Zhi, W.S. Origin of the Wunugetushan porphyry Cu–Mo deposit, Inner Mongolia, NE China: Constraints from geology, geochronology, geochemistry, and isotopic compositions. *J. Asian Earth Sci.* **2016**, *117*, 208–224.
72. Taylor, H.P. The application of oxygen and hydrogen isotope studies to problems of hydrothermal alteration and ore deposition. *Econ. Geol.* **1974**, *69*, 843–883. [[CrossRef](#)]

**Disclaimer/Publisher’s Note:** The statements, opinions and data contained in all publications are solely those of the individual author(s) and contributor(s) and not of MDPI and/or the editor(s). MDPI and/or the editor(s) disclaim responsibility for any injury to people or property resulting from any ideas, methods, instructions or products referred to in the content.